CORA Cork Open Research Archive
Cartlann Taighde Oscailte Chorcaí

Title	Modeling scattering matrix containing evanescent modes for wavefront shaping applications in disordered media
Authors	Raju, Michael;Jayet, Baptiste;Andersson-Engels, Stefan
Publication date	2026-07-29
Original Citation	Raju, M, Jayet, B & Andersson-Engels, S 2026, 'Modeling scattering matrix containing evanescent modes for wavefront shaping applications in disordered media', Physical Review Research, vol. 8, no. 3, 033123, pp. 1-16. https://doi.org/10.1103/86th-pl8q
Type of publication	Article (peer-reviewed)
Link to publisher's version	https://www.scopus.com/pages/publications/105046451268 - 10.1103/86th-pl8q
Rights	© 2026, the authors. Published by the American Physical Society under the terms of the Creative Commons Attribution 4.0 International license. Further distribution of this work must maintain attribution to the author(s) and the published article's title, journal citation, and DOI. - https://creativecommons.org/licenses/by/4.0/
Download date	2026-11-16 09:50:21
Item downloaded from	https://hdl.handle.net/10468/19199



University College Cork, Ireland
Coláiste na hOllscoile Corcaigh

Modeling scattering matrix containing evanescent modes for wavefront shaping applications in disordered media

Michael Raju [1,2,*] Baptiste Jayet [1] and Stefan Andersson-Engels [1,2]
[1]*Tyndall National Institute, Lee Maltings Complex, Dyke Parade, Cork T12 R5CP, Ireland*
[2]*School of Physics, University College Cork, College Road, Cork T12 K8AF, Ireland*

(Received 17 April 2024; accepted 8 June 2026; published 29 July 2026)

We developed an open-source scalar wave transport model to estimate the generalized scattering matrix (*S*-matrix) of a disordered medium in the diffusion regime. The term *generalized* refers to the incorporation of evanescent wave field modes alongside propagating modes in the estimation of the *S*-matrix. To achieve this, we employed the scalar Kirchhoff-Helmholtz boundary integral formulation together with the Green's function perturbation method, thereby extending the conventional Fisher-Lee relations to include evanescent modes. The estimated *S*-matrix, which satisfies the generalized unitarity and reciprocity relations, is modeled for a two-dimensional disordered waveguide. The generalized transmission matrix contained within the *S*-matrix is utilized to estimate the optimal phase-conjugate wavefront for focusing onto an evanescent mode. The phenomenon of a universal transmission value of 2/3 for such an optimal phase conjugate wavefront is demonstrated in the context of evanescent wave mode focusing through a diffusive disorder. The presented code framework may be of interest to wavefront shaping researchers for visualizing and estimating wave transport properties in general.

DOI: 10.1103/86th-pl8q

I. INTRODUCTION

Coherent control [1] of waves in disordered media through wavefront shaping has been an actively researched topic across various domains of physics, including electromagnetics and acoustics. Experimental demonstrations of coherent control using light, such as focusing outside a disordered medium [2], enhancing total light transmission through a disorder [3,4], and focusing light within a region enclosed by disorder [5], have been reported. Preferential deposition [6–8] of energy within a disordered medium has also emerged as an application in the field of coherent light control. The availability of wave-shaping devices, such as spatial light modulators, has significantly advanced research on coherent control experiments using light, particularly through the use of optical [9] transmission matrix. For a comprehensive study of the transport aspects in these wavefront shaping applications, modeling the scattering matrix (*S*-matrix) is particularly advantageous.

To estimate the regular *S*-matrix containing only the propagating wave modes for wavefront shaping applications, the Green's function perturbation method, combined with the conventional Fisher-Lee relations [1,10], is used. This approach is commonly employed to validate wavefront shaping experiments [3,4,11,12] that involve only propagating wave modes. A waveguidelike geometry, often associated with the Landauer formalism for electronic conduction [13], is typically adopted for such validations. On the other hand, accounting for evanescent wave modes is experimentally significant in the context of wavefront shaping for achieving subwavelength resolution during focusing [14,15]. These experiments involving the focusing of evanescent wave modes are supported and motivated by the original proposal of the generalized *S*-matrix by Carminati *et al.* [16] and the associated description of its unitarity and reciprocity properties. Here, the term *generalized* refers to the inclusion of evanescent modes alongside conventional propagating modes in the estimation of the *S*-matrix. The overarching goals of this paper are (1) to describe the method used for numerically estimating the generalized *S*-matrix proposed by Carminati *et al.* [16] for a disordered medium in the Landauer-waveguide geometry and (2) to combine the statistical analysis of scattered propagating and evanescent modes under this generalized modeling framework, particularly targeting wavefront shaping applications. Additionally, the classical wave scattering methods presented in the paper are implemented in matlab® and made available to readers as an open-source code package, accompanied by its user manual. Interested readers can use the code not only for the numerical estimation of the generalized *S*-matrix, but also for the visualization of wave transport within the medium, especially involving propagating eigenchannels.

Several numerical approaches are already available to model electromagnetic scattering in disordered media and can, in principle, be used to estimate the scattering matrix. The finite-difference time-domain (FDTD) method, which solves Maxwell's equations on a spatial grid, has been used to numerically construct transmission matrices and extract eigenchannels in disordered slabs [17]. However, FDTD re-

*Contact author: michaelraju@umail.ucc.ie

Published by the American Physical Society under the terms of the Creative Commons Attribution 4.0 International license. Further distribution of this work must maintain attribution to the author(s) and the published article's title, journal citation, and DOI.

quires a fine spatial grid, which becomes memory intensive for large three-dimensional domains. Therefore, the pseudospectral time-domain (PSTD) method [18] addresses this by replacing finite differences with Fourier-based spatial derivatives, reducing the required grid density to approximately two points per wavelength and enabling full three-dimensional solutions for macroscopic random media. Both FDTD and PSTD discretize the entire computational volume, which can increase the memory requirement. The discrete dipole approximation (DDA) offers an alternative by representing the scattering medium as a collection of polarizable dipoles rather than a uniform grid, and a systematic comparison of DDA and PSTD has shown that their relative performance depends strongly on the particle size parameter and refractive index contrast [19]. Extending the dipole framework to large-scale inhomogeneous slabs, the coupled dipole approximation (CDA) treats the medium as a self-consistent system of polarizable dipoles interacting through a modified slab Green's function [20]. When the medium consists of discrete identifiable scatterers rather than a continuous random permittivity, the superposition T-matrix method [21] provides an alternative route to determine numerically exact solutions by combining analytical single-particle T-matrices with interparticle coupling to account for multiple scattering. All of the above methods simulate a specific realization of the disordered medium. A conceptually different strategy is offered by random matrix theory [22], which instead characterizes the probability distribution of scattering matrix elements across an ensemble of disorder realizations by exploiting single-particle scattering properties and the asymptotic Gaussian statistics of random phasor sums in the limit of many scatterers. They obtain the scattering matrix of thicker systems by cascading transfer matrices of individually thin slabs, considering only propagating modes. Physical constraints such as reciprocity and unitarity are ensured within their statistical model, with extensions to polarized light [22]. While all the methods discussed above scale favorably with the number of scatterers or discretization points, the electromagnetic propagation methods (FDTD, PSTD, DDA, CDA, and T-matrix) offer limited analytical tractability regarding the structure of the scattering matrix and its estimation. In particular, symmetry properties are typically checked numerically rather than derived at the level of the formulation. Furthermore, in all of the above approaches, although evanescent fields may be present within the medium during computation in some cases, the scattering matrices that can potentially be estimated are assembled predominantly in the basis of propagating modes. Evanescent mode contributions are typically discarded before or during the construction of the transmission matrix.

In the present work, we employ the Green's function perturbation method and generalize the conventional Fisher-Lee relations to incorporate evanescent modes. This approach is computationally more demanding than the methods above due to the necessity of storing and perturbing the Green's functions involved. For example, the computational complexity of the direct inversion of the Dyson's system of equations (see Sec. III A in the Supplemental Material [24]) scales as $\mathcal{O}(N_p^3)$ in the number of discretization points N_p. Even though the iterative method of solving the perturbation system of equations fully, which is the method we adopted in this paper (see Sec. III B in the Supplemental Material [24]), reduces the computational complexity to a subcubic level, the memory requirement to store the Green's function is relatively higher compared to the previously cited works. This makes our approach generally less suited to very large-scale three-dimensional disordered systems. However, we circumvent that issue by breaking a large medium into thinner slabs and using the S-matrix cascading rule involving the generalized S-matrix containing evanescent modes to estimate the effective S-matrix of the larger system. In addition to this, our method offers several analytical advantages that are central to the goals of this work. The generalized Fisher-Lee relations yield closed-form S-matrix elements including the evanescent modes, enabling analytical tractability and explicit analytical verification of symmetry relations such as reciprocity. It provides an accurate S-matrix for a given disorder realization as it is based on numerical perturbation method. The perturbed Green's function provides direct access to the internal field distribution throughout the medium for any arbitrary input, including the visualization and estimation of eigenchannels.

In this context, the key novelties and contributions of this paper are summarized as follows. First, the conventional Fisher-Lee relations are extended to include evanescent modes, enabling the construction of a generalized S-matrix that consistently incorporates both propagating and evanescent wave contributions. Second, this generalized framework provides a rigorous basis for modeling wavefront shaping scenarios involving subwavelength focusing enabled by evanescent waves. Third, it is shown that the universal $2/3$ optimal transmission rule, well established for propagating modes in diffusive media, remains valid for the background transmission associated with evanescent wave focusing. Finally, the generalized S-matrix formalism enables the cascading of S-matrices corresponding to thin layers of the disordered medium, allowing thicker systems to be constructed efficiently. By breaking the medium into slices, this approach makes it possible to compute wave transport for arbitrary sample thicknesses on standard desktop computational resources.

The paper is organized as follows. First, Sec. II reviews the definitions of propagating and evanescent eigenmodes, along with the unperturbed and the disorder-perturbed Green's functions, which form the foundation for defining the S-matrix. For the disorder perturbation of the Green's function, spatially correlated disorders are employed, where the correlation length can be used to tailor transport properties. Once the perturbed Green's function is obtained, the Kirchhoff-Helmholtz boundary integral formulation of the wave scattering problem is discussed. Such a boundary integral formulation is used to estimate the generalized S-matrix from the perturbed Green's function. Additionally, the boundary integral equation enables the visualization of the total field for a given incident wave from the left or the right side of the disorder and validates the numerical correctness of the estimated generalized S-matrix. Next, Sec. III presents the direct estimation of the generalized S-matrix components from the perturbed Green's function, resulting in the generalization of the conventional Fisher-Lee relations. To ensure the numerical correctness of the code implementation, the estimated S-matrix is shown to satisfy the generalized unitarity and reciprocity relations in Sec. IV.

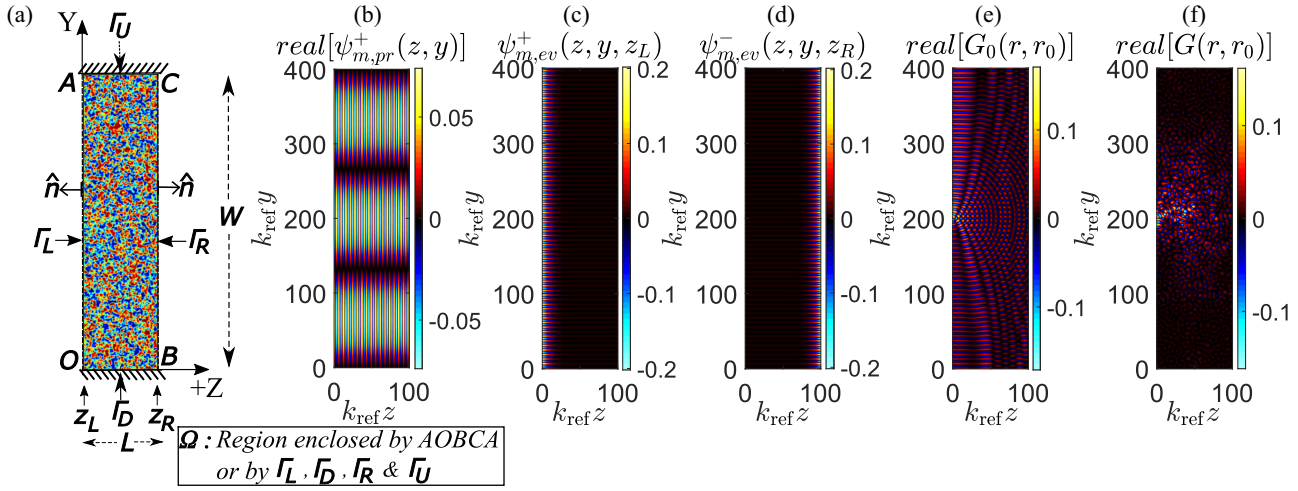


FIG. 1. The waveguidelike geometry of the computational domain and the plots of the real parts of eigenmodes, unperturbed and perturbed Green's functions. (a) Geometry of the computational domain. Boundary around the diffusive disorder (*AOBCA*) is denoted by Γ, which is the union of four boundary segments Γ_L, Γ_D, Γ_R, and Γ_U, where L stands for left, R stands for right, U stands for up, and D for down sides of the disorder. The 2D region enclosed by Γ is referred to as Ω. Transverse boundaries Γ_U and Γ_D have reflection (mirror) boundary conditions. The transverse size of the slab is W and the longitudinal thickness is L. (b) Real part of mth eigenmode, which is a propagating (pr) eigenmode. In this example, $m = 3$, out of the $M_{\text{pr}} = 130$ propagating modes possible for the given $k_{\text{ref}}W$. The $+$ symbol in the superscript denotes that the wave is propagating rightward along $+z$ direction. The discrete form (Sec. II of the Supplemental Material [24]) of the analytical equation given in Eq. (2) is used for plotting. (c) An evanescent eigenmode, plotted using Eq. (6a) for $m = 132$, being the second evanescent mode out of the $M_{\text{ev}} = 30$ evanescent modes taken. Here, the evanescent mode is incident rightward (with a superscript $+$) originating from the boundary Γ_L at z_L. Similarly, the left-going scattered evanescent eigenmode exist at Γ_L in the presence of disorder, although not plotted here. (d) An evanescent eigenmode [plotted using Eq. (6b) for $m = 132$] incident leftward (with a superscript $-$) originating from Γ_R at z_R. Similarly, the right-going scattered evanescent mode exist at Γ_R in the presence of disorder, although not plotted here. (e) Real part of the disorderless Green's function $G_0(z, y, z_0, y_0)$ for $(k_{\text{ref}}z_0, k_{\text{ref}}y_0)$ at (0, 201.46). Discrete form of Eq. (8) is used for plotting, where 30 evanescent modes are used in addition to all the 130 propagating modes. (f) Similarly, plotting the perturbed Green's function $G(r, r_0)$ [corresponding to the disorder given in Fig. 2(b)] estimated by solving the Dyson's equation [Eq. (9)] as given in Sec. III of the Supplemental Material [24].

These relations are also crucial for discussing the properties of focusing onto an evanescent mode via phase conjugation of the transmitted propagating wave. Section V discusses the role of the number of evanescent modes accounted, disorder correlation length, and their impact on numerical resolution and computational cost. Toward the final portion of the paper (Sec. VI), the scenario of wavefront shaping involving the focusing onto an evanescent mode in transmission and its associated properties, particularly the universal background transmission, is studied. The formation of a nonzero background intensity while focusing is well studied [23] in the case involving only propagating modes. To maintain the conciseness of the paper, Supplemental Material [24] is provided, containing derivations of some of the results presented.

II. DEFINITIONS AND NOTATIONS USED FOR THE BOUNDARY INTEGRAL FORMULATION

The paper addresses the two-dimensional (2D) scalar Helmholtz wave equation without loss or gain, given as

$$\left[\nabla^2 + k_0^2 \mu_r \tilde{\epsilon}_r(r)\right]\tilde{E}(r) = 0, \tag{1}$$

where $\tilde{E}(r)$ represents the complex-valued 2D scalar wave field as a function of the position $r = (z, y)$, $k_0 = 2\pi/\lambda_0$ is the free-space wave vector magnitude, λ_0 is the free-space wavelength, $\tilde{\epsilon}_r(r)$ is the relative dielectric permittivity constant (as a function of the position) forming the scattering strength of the random media, and μ_r (taken as unity) is the relative permeability constant. The time-harmonic dependence of $\tilde{E}(r)$ is implicitly taken as $e^{-i\omega_0 t}$, where i is the imaginary unit and ω_0 is the angular temporal frequency. The disorder dielectric constant $\tilde{\epsilon}_r(r)$ is defined as a spatially dependent perturbation $\delta\tilde{\epsilon}_r(r)$ added to a uniform reference (background) dielectric constant $\tilde{\epsilon}_r^{\text{ref}}$ as $\tilde{\epsilon}_r(r) = \tilde{\epsilon}_r^{\text{ref}} + \delta\tilde{\epsilon}_r(r)$. In this paper, $\delta\tilde{\epsilon}_r(r)$ is taken to be spatially correlated. A description of the generation of spatially correlated disorder used for the modeling can be found in Sec. I of the Supplemental Material [24]. Although uncorrelated disorders with very small correlation length l_c (approaching zero) are analytically and computationally simpler to implement, random media such as biological tissue samples involve nonzero spatial correlation lengths [25]. If $\delta\tilde{\epsilon}_r(r) = 0$, the wave equation for the disorder-free region simplifies to $[\nabla^2 + k_{\text{ref}}^2]\tilde{E}(r) = 0$, where $k_{\text{ref}}^2 = k_0^2\tilde{\epsilon}_r^{\text{ref}}$ such that $k_{\text{ref}} = k_0\eta_{\text{ref}}$. Here, k_{ref} is the magnitude of the wave vector in a spatially uniform reference dielectric medium and $\eta_{\text{ref}} = \sqrt{\tilde{\epsilon}_r^{\text{ref}}}$ is the refractive index of the reference medium.

Completely reflecting (mirror) boundary conditions at the transverse boundaries [at $y = 0$ and $y = W$ in Fig. 1(a)] were implemented to facilitate the accounting of the flux conservation just at the left and the right longitudinal boundaries (at $z = z_L$ and $z = z_R$). The subscripts L and R on the boundary Γ denote the left and the right boundaries, respectively, as shown in Fig. 1(a). With respect to the geometry shown in Fig. 1(a), without any disorder, one can define both prop-

agating eigenmodes [shown in Fig. 1(b)] and evanescent eigenmodes [shown in Figs. 1(c) and 1(d)]. These eigenmodes are the orthonormal basis wave states, forming the modal basis with which any arbitrary wave in the computational domain can be expressed as a basis expansion. The S-matrix is defined with respect to these eigenmode basis wave states, where the wave field modes can be propagating (pr) or evanescent (ev) in general. Conventionally, the right-traveling (along $+z$ direction) or the left-traveling (along $-z$ direction) propagating eigenmodes are combinedly defined as

$$\psi^{\pm}_{m,\mathrm{pr}}(z,y) = \phi^{\pm}_{m,\mathrm{pr}}(z)\chi_m(y), \tag{2}$$

where $\phi^{\pm}_{m,\mathrm{pr}}(z)$ and $\chi_m(y)$ are given as

$$\phi^{\pm}_{m,\mathrm{pr}}(z) = \frac{1}{\sqrt{k_z^{(m)}}} e^{\pm i k_z^{(m)} z}, \tag{3}$$

$$\chi_m(y) = \sqrt{\frac{2}{W}} \sin\left(k_y^{(m)} y\right), \tag{4}$$

such that $k_y^{(m)} = m\pi/W$ is the transverse wave vector component of the mth eigenmode along the y direction and $k_z^{(m)}$ is the real longitudinal wave vector component of the mth eigenmode along the z direction. The "+" symbol in the superscript of $\phi^{+}_{m,\mathrm{pr}}(z,y)$ and $\psi^{+}_{m,\mathrm{pr}}(z,y)$ denotes wave propagation along the $+z$ direction (from the left to the right of the computational domain), while the "−" symbol denotes the propagation along the $-z$ direction (from the right to the left). Here, the function $\chi_m(y)$ represents the transverse component of the eigenmode, satisfying the mirror (reflection) boundary conditions (at $y = 0$ and $y = W$), with W being the transverse size of the computational region, as shown in the Fig. 1(a). The index (m) in the superscript of $k_y^{(m)}$ denotes the positive integer index for the mth wave vector. (m) is a positive integer due to the discrete nature of $k_y^{(m)}$, which arises from the transverse reflecting boundary condition. An example for a propagating eigenmode is plotted in Fig. 1(b), where $m = 3$ and the wave propagates rightward. $\chi_m(y)$ satisfies the orthogonality relationship $\langle\chi_m(y)|\chi_n(y)\rangle = \delta_{\mathrm{kron}}(m,n)$, where δ_{kron} is the Kronecker delta function. There are approximately $2\eta_{\mathrm{ref}}W/\lambda_0$ propagating eigenmodes. The wave vector components $k_y^{(m)}$ and $k_z^{(m)}$ obey the dispersion relation $(k_y^{(m)})^2 + (k_z^{(m)})^2 = k_{\mathrm{ref}}^2$, where $k_{\mathrm{ref}} = 2\pi\eta_{\mathrm{ref}}/\lambda_0 = \omega_0\eta_{\mathrm{ref}}/c$.

For the evanescent modes,

$$k_z^{(m)} = \sqrt{k_{\mathrm{ref}}^2 - \left(k_y^{(m)}\right)^2} = i k_{z,\mathrm{ev}}^{(m)}, \tag{5}$$

where $k_z^{(m)}$ are purely imaginary and $k_{z,\mathrm{ev}}^{(m)}$ are real numbers. The left- and right-going evanescent eigenmodes are defined to originate relative to the two boundaries Γ_L and Γ_R [boundaries shown in the Fig. 1(a) at z_L and z_R], positioned close to the disorder. These evanescent modes attenuate along the direction of incidence onto the disorder from either the left or right side of the disorder and also attenuate when scattered away. The evanescent modes are defined as follows, with dependence on z_L or z_R:

$$\psi^{\pm}_{m,\mathrm{ev}}(z,y,z_L) = \phi^{\pm}_{m,\mathrm{ev}}(z,z_L)\chi_m(y), \tag{6a}$$

$$\psi^{\pm}_{m,\mathrm{ev}}(z,y,z_R) = \phi^{\pm}_{m,\mathrm{ev}}(z,z_R)\chi_m(y), \tag{6b}$$

where

$$\phi^{\pm}_{m,\mathrm{ev}}(z,z_L) = \frac{1}{\sqrt{|k_z^{(m)}|}} e^{-k_{z,\mathrm{ev}}^{(m)}|z-z_L|}, \tag{7a}$$

$$\phi^{\pm}_{m,\mathrm{ev}}(z,z_R) = \frac{1}{\sqrt{|k_z^{(m)}|}} e^{-k_{z,\mathrm{ev}}^{(m)}|z-z_R|}. \tag{7b}$$

The symbol "±" on the left-hand side of Eq. (7) indicates the directions of incidence/scattering of the evanescent mode originating relative to z_L or z_R (with "+" for rightward and "−" for leftward emergence). Note that "±" does not appear on right-hand side of Eq. (7), as both the leftward- and rightward-emerging modes attenuate away from z_L or z_R along z. Two examples of the incident evanescent modes are shown in Figs. 1(c) and 1(d), illustrating a right-going evanescent eigenmode at Γ_L and a left-going evanescent eigenmode at Γ_R, respectively. Although not plotted, scattered evanescent modes from the disorder also exist, which are left going at Γ_L and a right going at Γ_R.

The eigenmodes, referred to as ψ_m in general, include a normalization factor $1/\sqrt{|k_z^{(m)}|}$. For the propagating modes, $1/\sqrt{k_z^{(m)}}$ ensures that the flux (current) component flowing normal to a given boundary region Γ_L or Γ_R is unity. The flux density of the mth eigenmode is defined as $\vec{J}^{(m)}(z,y) = J_z^{(m)}(r)\hat{e}_z + J_y^{(m)}(r)\hat{e}_y = \Im\mathfrak{m}\{\psi_m^*\nabla\psi_m\}$, where $\hat{e}_z$ and $\hat{e}_z$ are unit vectors along the Z and Y directions, respectively, and $\Im\mathfrak{m}$ refers to the imaginary part. As there is no flux crossing the transverse boundaries Γ_U and Γ_D, $J_y^{(m)}(r)$ is zero along the boundary normal. For the evanescent modes, as there is no flux crossing the boundaries, there is no physical necessity for defining a normalization factor. Nevertheless, a normalization factor $1/\sqrt{|k_z^{(m)}|} = 1/\sqrt{k_{z,\mathrm{ev}}^{(m)}}$ is included in the definition of the evanescent eigenmodes. This is primarily for the convenience of modeling, ensuring that the propagating modes and the evanescent modes are of the same numerical order of magnitude. This avoids precision errors when estimating the S-matrix.

Next, using the propagating and evanescent eigenmodes, the analytical expression [26] for the 2D Green's function $G_0(r,r_0)$ [plotted in Fig. 1(e)] without any disorder perturbation is given as

$$G_0(z,y,z_0,y_0) = \sum_{m=1}^{\infty} \frac{1}{2ik_z^{(m)}} e^{ik_z^{(m)}|(z-z_0)|} \sqrt{\frac{2}{W}} \times \sin\left(k_y^{(m)} y\right)\sqrt{\frac{2}{W}} \sin\left(k_y^{(m)} y_0\right), \tag{8}$$

where $r_0 = (z_0, y_0)$ is the source location, $k_z^{(m)}$ is real for the propagating terms in the summation, and $k_z^{(m)} = i k_{z,\mathrm{ev}}^{(m)}$ is imaginary for the evanescent components. Although the summation in Eq. (8) runs from $m = 1$ to infinity, it is truncated to include all M_{pr} propagating modes, where $M_{\mathrm{pr}} \approx 2\eta_{\mathrm{ref}}W/\lambda_0$, and a certain truncation number of evanescent modes, M_{ev}. As an example, in this paper, M_{ev} is set as 30, $M_{\mathrm{pr}} = 130$, and $M_{\mathrm{total}} = M_{\mathrm{pr}} + M_{\mathrm{ev}}$. Considerations to be taken for choosing this truncation number for the evanescent modes are described in Sec. V for a given spatially correlated disorder realization. Thus, the summation in Eq. (8) runs from $m = 1$ to $m = M_{\mathrm{total}}$ for the numerical implementation of $G_0(r,r_0)$ in the code.

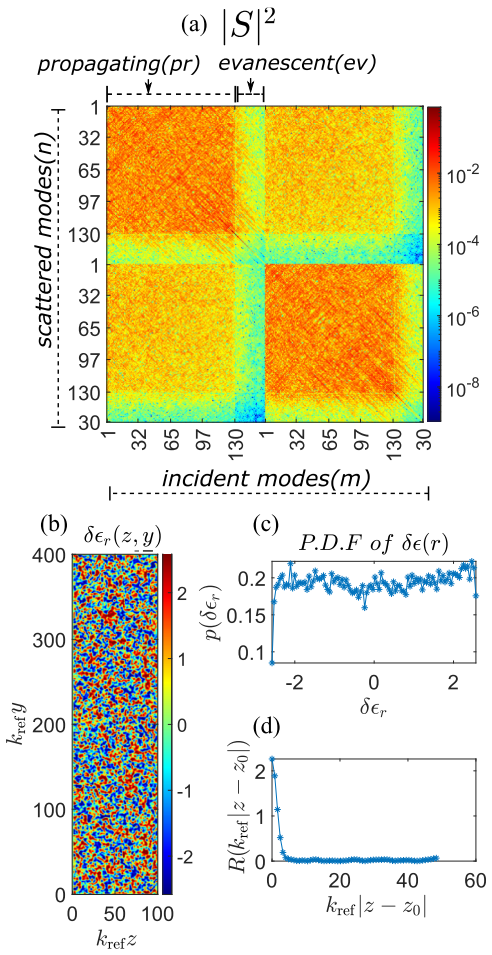


FIG. 2. ***S***-matrix of a diffusive spatially correlated disorder with average transmission $\langle\tau_{21}^{\text{pr,pr}}\rangle = 0.198$. (a) Squared magnitude of the S-matrix given in Eq. (20) (plotted in log scale) estimated using the generalized Fisher-Lee relations given in Tables I, III, IV, and V. The number of propagating modes (M_{pr}) involved for wave incidence and scattering is 130 and the number of evanescent modes (M_{ev}) is 30 for the quasi-one-dimensional (quasi-1D) geometry. As an example, the $\mathbf{S}_{11}$ portion of the S-matrix contains both propagating and evanescent wave modes where the propagating modes appear first in the matrix (with respect to row and column indices) followed by the evanescent modes. (b) Spatially correlated disorder used for the estimation of the S-matrix. The disorder is represented by the dielectric-constant perturbation $\delta\epsilon_r(z,y)$, modeled as per Sec. I A of the Supplemental Material [24]. (c) Probability density function of the disorder $\delta\epsilon_r(z,y)$ matrix elements such that the var$(\delta\epsilon_r) = 2.26$. (d) Spatial correlation function $R(k_{\text{ref}}|z-z_0|)$, defined in Eq. (1) of Sec. I A of the Supplemental Material [24], is plotted where the dimensionless spatial correlation length $k_{\text{ref}}l_c$ along z axis is 2.01.

Using $G_0(r,r_0)$ and the dielectric disorder perturbation $\delta\tilde{\epsilon_r}(r)$ [shown in Fig. 2(b)], the perturbed Green's function $G(r,r_0)$ [plotted in Fig. 1(f)] is estimated using Dyson's equation [13,27], as given below:

$$G(r,r_0) = G_0(r,r_0) + \int_{r_1} G_0(r,r_1)V(r_1)G(r_1,r_0)dr_1, \quad (9)$$

where $V(r) = -k_0^2\delta\tilde{\epsilon_r}(r)$ is the scattering potential at the position r. Dyson's integral equation is solved in this paper by generalizing the method given in Refs. [28,29], solving for a block of scattering particles taken at once and iteratively updating the Green's function. For details on the method used to obtain $G(r,r_0)$, refer to Sec. III of the Supplemental Material [24]. As the propagating and the evanescent eigenmodes $\psi_m^{\pm}(r)$ form a complete basis set, the perturbed Green's function $G(r,r_0)$ can also be expanded in terms of these eigenmodes. On the left boundary, $G(r,r_0)$ can be expanded in terms of left-going eigenmodes, and on the right boundary, $G(r,r_0)$ can be expanded in terms of right-going eigenmodes. Hence, $G(r,r_0)$ satisfies the homogeneous boundary conditions given in Sec. IV of the Supplemental Material [24], which are also satisfied by the eigenmodes. These boundary conditions are useful for simplifying the analysis presented in the following section. The next section deals with the Kirchhoff-Helmholtz boundary integral formulation of the scattering problem, incorporating $G(r,r_0)$ and the total field around the boundary Γ. This is followed by the direct numerical estimation of the generalized S-matrix from $G(r,r_0)$. The goal of this section is to establish the relationship between the perturbed Green's function $G(z,y,z_0,y_0)$ and the total wave field $\tilde{E}(z,y)$ that exists inside and around a medium due to an arbitrary wave incident on the disorder. This relationship helps estimate the response of a random medium excited by an arbitrary incident wave.

First, consider the case of wave incidence on the disorder from the left side only, where $E^{\text{inc}}(z,y)$ (traveling from left to right) is the incident wave. On the left boundary Γ_L, the total wave field due to wave incidence only from the left side is given as

$$\tilde{E}(z,y)|_{(z,y)\in\Gamma_L} = \tilde{E}^{\text{inc}}(z,y)|_{(z,y)\in\Gamma_L} + \tilde{E}^{\text{refl}}(z,y)|_{(z,y)\in\Gamma_L}, \quad (10)$$

where $\tilde{E}^{\text{refl}}(z,y)|_{(z,y)\in\Gamma_L}$ is the reflected wave on Γ_L. $\tilde{E}^{\text{inc}}(z,y)$ and $\tilde{E}^{\text{refl}}(z,y)$ can be expanded in terms of eigenmodes and their associated complex coefficients on Γ_L as follows:

$$\begin{aligned}\tilde{E}^{\text{inc}}(z,y)|_{(z,y)\in\Gamma_L} &= \sum_{m=1}^{M_{\text{total}}} c_m^+\psi_m^+(z,y)|_{(z,y)\in\Gamma_L} \\ &= \sum_{m=1}^{M_{\text{total}}} c_m^+\chi_m(y)\phi_m^+(z)|_{(z,y)\in\Gamma_L}\end{aligned}$$

$$\text{such that } \phi_m^+(z) = \begin{cases}\phi_{m,\text{pr}}^+(z), & \text{when } m \leqslant M_{\text{pr}}, \\ \phi_{m,\text{ev}}^+(z,z_L), & \text{when } m > M_{\text{pr}},\end{cases} \quad (11)$$

where c_m^+ is the mth complex coefficient used to synthesize the incident wave in terms of eigenmodes propagating along the $+z$ direction. Similarly,

$$\begin{aligned}\tilde{E}^{\text{refl}}(z,y)|_{(z,y)\in\Gamma_L} &= \sum_{n=1}^{N_{\text{total}}} r_n^-\psi_n^-(z,y)\Big|_{(z,y)\in\Gamma_L} \\ &= \sum_{n=1}^{N_{\text{total}}} r_n^-\chi_n(y)\phi_n^-(z)\Big|_{(z,y)\in\Gamma_L}\end{aligned}$$

$$\text{such that } \phi_n^-(z) = \begin{cases}\phi_{n,\text{pr}}^-(z), & \text{when } n \leqslant N_{\text{pr}}, \\ \phi_{n,\text{ev}}^-(z,z_L), & \text{when } n > N_{\text{pr}},\end{cases}$$

$$r_n^- = \sum_{m=1}^{M_{\text{total}}} \mathbf{S}_{11}^{nm}c_m^+, \quad (12)$$

where $\mathbf{S}_{11}^{nm}$ are the elements of the generalized reflection matrix $\mathbf{S}_{11}$ for the wave incidence only from the left side of the disorder. Here, m as the index denotes the incident eigenmode number and n denotes the scattered eigenmode number.

On the right boundary Γ_R, only the transmitted wave $\tilde{E}^{\text{trans}}(z,y)|_{(z,y)\in\Gamma_R}$ exists for the scenario of wave incidence only from the left side of the disorder. Therefore, the total field on Γ_R is given as

$$\begin{aligned}\tilde{E}(z,y)|_{(z,y)\in\Gamma_R} &= \tilde{E}^{\text{trans}}(z,y)|_{(z,y)\in\Gamma_R} \\ &= \sum_{n=1}^{N_{\text{total}}} t_n^+ \phi_n^+(z)\chi_n(y)\Big|_{(z,y)\in\Gamma_R} \\ \text{such that}\quad \phi_n^+(z) &= \begin{cases}\phi_{n,\text{pr}}^+(z), & \text{when } n \leqslant N_{\text{pr}},\\ \phi_{n,\text{ev}}^+(z,z_R), & \text{when } n > N_{\text{pr}},\end{cases} \\ \text{and } t_n^+ &= \sum_{m=1}^{M_{\text{total}}} \mathbf{S}_{21}^{nm} c_m^+, \end{aligned} \tag{13}$$

where $\mathbf{S}_{21}^{nm}$ are the elements of the generalized transmission matrix $\mathbf{S}_{21}$ for wave incidence only from the left side of the disorder.

Inside the medium, the total field of the wave is denoted as $\tilde{E}(z,y)$ itself. Consider the Helmholtz equation for the Green's function and the total field as follows:

$$\left[\nabla^2 + k_0^2\tilde{\epsilon}_r(z,y)\right]G(z,y,z_0,y_0) = \delta(z,z_0)\delta(y,y_0), \tag{14}$$

$$\left[\nabla^2 + k_0^2\tilde{\epsilon}_r(z,y)\right]\tilde{E}(z,y) = 0, \tag{15}$$

where ∇^2 is the Laplacian operator with respect to the field position (z,y). In Eq. (14), (z_0,y_0) is the Dirac-delta source location. Multiplying Eq. (14) by $\tilde{E}(z,y)$ and Eq. (15) by $G(z,y,z_0,y_0)$, followed by subtraction and the application of the divergence theorem, the following Kirchhoff-Helmholtz boundary integral equation is obtained, as shown in Appendix A of Ref. [30]:

$$\begin{aligned}&\tilde{E}(z_0,y_0)|_{(z_0,y_0)\in\Omega} \\ &= \iint \nabla\cdot\left\{\tilde{E}(r)\nabla G(r,r_0) - G(r,r_0)\nabla\tilde{E}(r)\right\}dzdy \\ &= \int_\Gamma \left\{\tilde{E}(r)\nabla G(r,r_0) - G(r,r_0)\nabla\tilde{E}(r)\right\}\cdot\hat{n}d\Gamma, \end{aligned} \tag{16}$$

where r denotes (z,y) and r_0 denotes (z_0,y_0). Note that (z_0,y_0) now represents the location where the field is visualized, and it is no longer the source location. This is consistent with the reciprocity property of the Green's function, $G(r,r_0) = G(r_0,r)$. Since there is no flux crossing Γ_U and Γ_D, the boundary integral involves only the terms associated with Γ_L and Γ_R. The Kirchhoff-Helmholtz boundary integral equation implies that the total field $\tilde{E}(z_0,y_0)$ at a point (z_0,y_0) inside the closed region Ω bounded by Γ can be estimated if the value of $\tilde{E}(z,y)$, and the Green's function $G(z,y,z_0,y_0)$ together with its spatial derivatives, is known at the boundaries Γ_L and Γ_R. The boundary integral can be simplified (with the derivation provided in Sec. V of the Supplemental Material [24]) as follows. For the wave incidence only from the left to the right of the disorder (incidence onto Γ_L),

$$\begin{aligned}&\tilde{E}(z_0,y_0)|_{(z_0,y_0)\in\Omega} \\ &= \sum_{m=1}^{M_{\text{total}}} 2ik_z^{(m)} \int \tilde{E}_m^{\text{inc}}(z,y)G(z,y,z_0,y_0)|_{(z,y)\in\Gamma_L}dy, \end{aligned} \tag{17}$$

where $\tilde{E}_m^{\text{inc}}(z,y)|_{(z,y)\in\Gamma_L} = c_m^+\psi_m^+(z,y)|_{(z,y)\in\Gamma_L}$. Here, c_m^+ is the mth complex coefficient used to synthesize the incident wave in terms of eigenmodes propagating along the $+z$ direction.

Similarly, for wave incidence only from the right side of the disorder (incidence onto Γ_R), the equation is similar to that of Eq. (17), except that now $(z,y)\in\Gamma_R$ as follows:

$$\begin{aligned}&\tilde{E}(z_0,y_0)|_{(z_0,y_0)\in\Omega} \\ &= \sum_{m=1}^{M_{\text{total}}} 2ik_z^{(m)} \int \tilde{E}_m^{\text{inc}}(z,y)G(z,y,z_0,y_0)|_{(z,y)\in\Gamma_R}dy, \end{aligned} \tag{18}$$

where $\tilde{E}_m^{\text{inc}}(z,y)|_{(z,y)\in\Gamma_R} = c_m^-\psi_m^-(z,y)|_{(z,y)\in\Gamma_R}$. Similar to that of Eq. (11),

$$\tilde{E}^{\text{inc}}(z,y)|_{(z,y)\in\Gamma_R} = \sum_{m=1}^{M_{\text{total}}} c_m^-\psi_m^-(z,y)|_{(z,y)\in\Gamma_R}. \tag{19}$$

The simplified boundary integral equation (17) or (18), along with Eqs. (10) and (13), can be used for two purposes: (1) to estimate the generalized reflection ($\mathbf{S}_{11}$ and $\mathbf{S}_{22}$) and transmission ($\mathbf{S}_{21}$ and $\mathbf{S}_{12}$) matrices and (2) to visualize the total field $\tilde{E}(z_0,y_0)|_{(z_0,y_0)\in\Omega}$, for a given incident wave from the left side or the right side of the disorder. As an example, in Sec. VII of the Supplemental Material [24], the transmission eigenchannels associated with $\mathbf{S}_{21}^{\text{pr,pr}}$ and $\mathbf{S}_{12}^{\text{pr,pr}}$ are plotted using the boundary integral equations.

III. EXTENDED FISHER-LEE RELATIONS FOR ESTIMATING THE GENERALIZED *S*-MATRIX

This section explains how the boundary integral equations are used to estimate the generalized S-matrix where the traditional Fisher-Lee method [1,10,30,31] is generalized to include the evanescent wave modes as well. The definition of S-matrix is given as

$$\mathbf{S} = \begin{bmatrix}\mathbf{S}_{11} & \mathbf{S}_{12}\\ \mathbf{S}_{21} & \mathbf{S}_{22}\end{bmatrix}, \tag{20}$$

where $\mathbf{S}_{21}$ and $\mathbf{S}_{12}$ are the generalized transmission matrices for wave incidence from the left and right, respectively. Similarly, $\mathbf{S}_{11}$ and $\mathbf{S}_{22}$ are the generalized reflection matrices for wave incidence from the left and right, respectively. The size of the transmission matrix $\mathbf{S}_{21}$ is generally given as $[N_{\text{total}}\times M_{\text{total}}]$, where M_{total} is the total number of incident eigenmodes and N_{total} is the total number of transmitted eigenmodes. For the quasi-1D geometry shown in Fig. 1(a), $M_{\text{pr}} = N_{\text{pr}}$ and $M_{\text{ev}} = N_{\text{ev}}$. Due to the wave incidence only from the left side of the disorder onto the boundary Γ_L, there exists the total field composed of the incident wave and the

reflected wave on Γ_L. On the transmitted side, the total wave field consists of the transmitted wave. One can match the total field to the boundary integral equation and solve for $\mathbf{S}_{11}$ and $\mathbf{S}_{21}$ to obtain the generalized Fisher-Lee relations. Similarly, the estimation of $\mathbf{S}_{22}$ and $\mathbf{S}_{12}$ follows the same logic, where the wave incidence is only from the right side of the disorder. First, the methodology adopted for deriving the generalized $\mathbf{S}_{11}$ matrix elements is presented as follows.

The simplified boundary integral equation previously introduced in Eq. (17), where the wave incidence occurs only from the left side of the disorder, serves as the starting point for deriving the $\mathbf{S}_{11}$ matrix elements. As the left-hand side of Eq. (17) denotes the total field due to the wave incidence only from the left, one can estimate the total field on the left boundary. Substituting Eq. (10) into the left-hand side of Eq. (17), the following is obtained:

$$\{\tilde{E}^{\text{inc}}(z_0, y_0) + \tilde{E}^{\text{refl}}(z_0, y_0)\}|_{(z_0,y_0)\in\Gamma_L} = \sum_{m=1}^{M_{\text{total}}} \left\{ 2ik_z^{(m)} \int \tilde{E}_m^{\text{inc}}(z, y) G(z, y, z_0, y_0) dy \right\} \Big|_{\{(z,y)\&(z_0,y_0)\}\in\Gamma_L}. \tag{21}$$

Substituting the eigenmode basis expansion of a given incident wave $\tilde{E}^{\text{inc}}(z_0, y_0)$ and reflected wave $\tilde{E}^{\text{refl}}(z_0, y_0)$, as given in Eqs. (11) and (12), respectively, into Eq. (21), and using the property of the Kronecker delta function, the following is obtained:

$$\begin{aligned} &\sum_{n=1}^{N_{\text{total}}} \sum_{m=1}^{M_{\text{total}}} \left\{ c_n^+ \phi_n^+(z_0) \chi_n(y_0) \delta_{\text{kron}}(n, m)\big|_{(z_0,y_0)\in\Gamma_L} + c_m^+ \mathbf{S}_{11}^{nm} \chi_n(y_0) \phi_n^-(z_0)\big|_{(z_0,y_0)\in\Gamma_L} \right\} \\ &= \sum_{m=1}^{M_{\text{total}}} \left\{ 2ik_z^{(m)} \int c_m^+ \phi_m^+(z) \chi_m(y) G(z, y, z_0, y_0) dy \right\} \Big|_{\{(z,y)\&(z_0,y_0)\}\in\Gamma_L}. \end{aligned} \tag{22}$$

Since Eq. (22) holds for any incident wave represented by any set of c_m^+ values, one can collect the terms multiplied by c_m^+ and spanned by $\sum_{m=1}^{M_{\text{total}}}$ on both the left-hand side and right-hand side, and solve for $\mathbf{S}_{11}^{nm}$. Equation (22) then implies the following:

$$\begin{aligned} &\sum_{n=1}^{N_{\text{total}}} \phi_n^+(z_0) \chi_n(y_0) \delta_{\text{kron}}(n, m)\Big|_{(z_0,y_0)\in\Gamma_L} + \sum_{n=1}^{N_{\text{total}}} \mathbf{S}_{11}^{nm} \chi_n(y_0) \phi_n^-(z_0)\Big|_{(z_0,y_0)\in\Gamma_L} \\ &= 2ik_z^{(m)} \phi_m^+(z) \int \chi_m(y) G(z, y, z_0, y_0) dy|_{(z,y)}(z_0, y_0) \in \Gamma_L. \end{aligned} \tag{23}$$

To obtain an expression for $\mathbf{S}_{11}^{nm}$ using Eq. (23), the orthogonality relation involving $\chi_{n'}(y)$ is invoked as the next step. Upon multiplying both sides of Eq. (23) by $\chi_{n'}(y_0)$ and integrating with respect to y_0 yields the following:

$$\phi_{n'}^+(z_0) \delta_{\text{kron}}(n', m) + \mathbf{S}_{11}^{n'm} \phi_{n'}^-(z_0) = 2ik_z^{(m)} \phi_m^+(z) \iint \chi_m(y) G(z, y, z_0, y_0) \chi_{n'}(y_0) dy_0 dy, \tag{24}$$

where (z, y) and $(z_0, y_0) \in \Gamma_L$. For further simplification of Eq. (24), define the integral that appears on the right-hand side as follows:

$$G_{nm}^{\mathbf{S}_{11}} = \iint \chi_m(y) G(z, y, z_0, y_0) \chi_n(y_0) dy dy_0|_{(z,y)\&(z_0,y_0)\in\Gamma_L}. \tag{25}$$

Here, $G_{nm}^{\mathbf{S}_{11}}$ can be interpreted as a Fourier-like decomposition in the eigenspace, of the Green's function component used for estimating $\mathbf{S}_{11}^{nm}$. By renaming n' as n, setting the positions of z and z_0 on Γ_L to 0, and using $G_{nm}^{\mathbf{S}_{11}}$, Eq. (24) can be simplified as

$$\begin{aligned} &\phi_n^+(z_0 = 0) \delta_{\text{kron}}(n, m) + \mathbf{S}_{11}^{nm} \phi_n^-(z_0 = 0) \\ &= 2ik_z^{(m)} \phi_m^+(z = 0) G_{nm}^{\mathbf{S}_{11}}. \end{aligned} \tag{26}$$

There are four different cases to further simplify Eq. (26) based on the nature of the incident modes (indexed by m) and reflected modes (indexed by n) as propagating or evanescent.

Case 1 is when both the incident and reflecting modes are propagating, such that $m \leqslant M_{\text{pr}}$ and $n \leqslant N_{\text{pr}}$. Substituting the expressions for the propagating $\phi_n^+(z_0 = 0)$, $\phi_n^-(z_0 = 0)$, and $\phi_m^+(z = 0)$ in Eq. (26), the following simplification is obtained:

$$\frac{1}{\sqrt{k_z^{(n)}}} \delta_{\text{kron}}(n, m) + \frac{\mathbf{S}_{11}^{nm}}{\sqrt{k_z^{(n)}}} = 2ik_z^{(m)} \frac{1}{\sqrt{k_z^{(m)}}} G_{nm}^{\mathbf{S}_{11}}, \tag{27}$$

which is used to derive the expressions for $\mathbf{S}_{11}^{nm}$ provided in the first row of Table I. In Table I, the terms under Inc(m) indicate the nature of the mth incident wave mode, and Refl(n) specifies the nature of the nth reflected wave mode, whether propagating (pr) or evanescent (ev).

Case 2 corresponds to the scenario where both the incident and reflected modes are evanescent, such that $m > M_{\text{pr}}$ and

TABLE I. Elements of $\mathbf{S}_{11}$.

Inc(m)	Refl(n)	$\mathbf{S}_{11}^{nm}$
pr	pr	$-\delta_{\text{kron}}(n, m) + 2i\sqrt{k_z^{(m)}}\sqrt{k_z^{(n)}} G_{nm}^{\mathbf{S}_{11}}$
ev	ev	$-\delta_{\text{kron}}(n, m) + -2\sqrt{\lvert k_z^{(m)}\rvert}\sqrt{\lvert k_z^{(n)}\rvert} G_{nm}^{\mathbf{S}_{11}}$
pr	ev	$2i\sqrt{k_z^{(m)}}\sqrt{\lvert k_z^{(n)}\rvert} G_{nm}^{\mathbf{S}_{11}}$
ev	pr	$-2\sqrt{\lvert k_z^{(m)}\rvert}\sqrt{k_z^{(n)}} G_{nm}^{\mathbf{S}_{11}}$

TABLE II. Integral forms of $G^{\mathbf{S}_{11}}_{nm}$, $G^{\mathbf{S}_{21}}_{nm}$, $G^{\mathbf{S}_{22}}_{nm}$, and $G^{\mathbf{S}_{12}}_{nm}$.

S-matrix estimation components	$G^{\mathbf{S}_{11}}_{nm}$, $G^{\mathbf{S}_{21}}_{nm}$, $G^{\mathbf{S}_{22}}_{nm}$, and $G^{\mathbf{S}_{12}}_{nm} = \iint \chi_m(y) G(z, y, z_0, y_0)\chi_n(y_0)dydy_0$ except for the change in the domains of integration as follows:		
$G^{\mathbf{S}_{11}}_{nm}$	$(z = 0, y) \in \Gamma_L$	and	$(z_0 = 0, y_0) \in \Gamma_L$
$G^{\mathbf{S}_{21}}_{nm}$	$(z = 0, y) \in \Gamma_L$	and	$(z_0 = z_R, y_0) \in \Gamma_R$
$G^{\mathbf{S}_{22}}_{nm}$	$(z = z_R, y) \in \Gamma_R$	and	$(z_0 = z_R, y_0) \in \Gamma_R$
$G^{\mathbf{S}_{12}}_{nm}$	$(z = z_R, y) \in \Gamma_R$	and	$(z_0 = 0, y_0) \in \Gamma_L$

$n > N_{\text{pr}}$. In this case, Eq. (26) simplifies as follows:

$$\frac{\delta_{\text{kron}}(n,m)}{\sqrt{|k_z^{(n)}|}} + \frac{\mathbf{S}^{nm}_{11}}{\sqrt{|k_z^{(n)}|}} = 2i\big(i|k_z^{(m)}|\big)\frac{1}{\sqrt{|k_z^{(m)}|}}G^{\mathbf{S}_{11}}_{nm}, \tag{28}$$

which is used to obtain the expression for $\mathbf{S}^{nm}_{11}$ given in the second row of Table I.

Case 3 corresponds to the scenario where the incident modes are propagating and the reflected modes are evanescent, such that $m \leqslant M_{\text{pr}}$ and $n > N_{\text{pr}}$. In this situation, $\delta_{\text{kron}}(n, m)$ in Eq. (26) becomes zero, where $M_{\text{pr}} = N_{\text{pr}}$. Simplifying Eq. (26) for Case 3 leads to the following:

$$\frac{\mathbf{S}^{nm}_{11}}{\sqrt{|k_z^{(n)}|}} = 2ik_z^{(m)}\frac{1}{\sqrt{k_z^{(m)}}}G^{\mathbf{S}_{11}}_{nm}, \tag{29}$$

which yields the expression for $\mathbf{S}^{nm}_{11}$ given in the third row of Table I.

Finally, Case 4 considers the scenario where the incident modes are evanescent and the reflected modes are propagating, such that $m > M_{\text{pr}}$ and $n \leqslant N_{\text{pr}}$. In this case, Eq. (26) simplifies as follows:

$$\mathbf{S}^{mn}_{11}\frac{1}{\sqrt{k_z^{(n)}}} = 2i\big(i|k_z^{(m)}|\big)\frac{1}{\sqrt{|k_z^{(m)}|}}G^{\mathbf{S}_{11}}_{nm}, \tag{30}$$

which provides the expression for $\mathbf{S}^{mn}_{11}$ given in the fourth row of Table I. The same method is applied to estimate the elements of $\mathbf{S}_{21}$. In this case, the boundary integral equation [Eq. (21)] takes the following form for $\mathbf{S}_{21}$:

$$\begin{aligned}\tilde{E}^{\text{trans}}(z_0, y_0)|_{(z_0,y_0)\in\Gamma_R} &= \sum_{m=1}^{M_{\text{total}}}\left\{2ik_z^{(m)}\int \tilde{E}^{\text{inc}}_m(z, y)G(z, y, z_0, y_0)dy\right\} \\ &\times\Big|_{(z,y)\in\Gamma_L\&(z_0,y_0)\in\Gamma_R},\end{aligned} \tag{31}$$

TABLE III. Elements of $\mathbf{S}_{21}$.

Inc(m)	Trans(n)	$\mathbf{S}^{nm}_{21}$
pr	pr	$2i\sqrt{k_z^{(m)}}\sqrt{k_z^{(n)}}e^{-iz_Rk_z^{(n)}}G^{\mathbf{S}_{21}}_{nm}$
ev	ev	$-2\sqrt{\lvert k_z^{(m)}\rvert}\sqrt{\lvert k_z^{(n)}\rvert}G^{\mathbf{S}_{21}}_{nm}$
pr	ev	$2i\sqrt{k_z^{(m)}}\sqrt{\lvert k_z^{(n)}\rvert}G^{\mathbf{S}_{21}}_{nm}$
ev	pr	$-2\sqrt{\lvert k_z^{(m)}\rvert}\sqrt{k_z^{(n)}}e^{-iz_Rk_z^{(n)}}G^{\mathbf{S}_{21}}_{nm}$

TABLE IV. Elements of $\mathbf{S}_{22}$.

Inc(m)	Refl(n)	$\mathbf{S}^{nm}_{22}$
pr	pr	$-\delta_{\text{kron}}(n,m)e^{-iz_R(k_z^{(m)}+k_z^{(n)})}$ $+2i\sqrt{k_z^{(n)}}\sqrt{k_z^{(m)}}e^{-iz_R(k_z^{(m)}+k_z^{(n)})}G^{\mathbf{S}_{22}}_{nm}$
ev	ev	$-\delta_{\text{kron}}(n,m) + -2\sqrt{\lvert k_z^{(m)}\rvert}\sqrt{\lvert k_z^{(n)}\rvert}G^{\mathbf{S}_{22}}_{nm}$
pr	ev	$+2i\sqrt{k_z^{(m)}}\sqrt{\lvert k_z^{(n)}\rvert}e^{-iz_Rk_z^{(m)}}G^{\mathbf{S}_{22}}_{nm}$
ev	pr	$-2\sqrt{\lvert k_z^{(m)}\rvert}\sqrt{k_z^{(n)}}e^{-iz_Rk_z^{(n)}}G^{\mathbf{S}_{22}}_{nm}$

where the transmitted wave field is evaluated at the right boundary, denoted by $(z_0, y_0) \in \Gamma_R$, and the wave incidence occurs on the left boundary, denoted by $(z, y) \in \Gamma_L$. As done previously, the eigenmode expansion for the incident and the transmitted waves, given in Eqs. (11) and (13), respectively, can be substituted into Eq. (31). Following the same procedure outlined for deriving Eqs. (22) and (23), the following equation is obtained for estimating $\mathbf{S}^{nm}_{21}$:

$$S^{nm}_{21}\phi_n^+(z_0 = z_R) = 2ik_z^{(m)}\phi_m^+(z = 0)G^{\mathbf{S}_{21}}_{nm}, \tag{32}$$

where

$$G^{\mathbf{S}_{21}}_{nm} = \iint \chi_m(y)G(z, y, z_0, y_0)\chi_n(y_0)dydy_0, \tag{33}$$

such that $(z = 0, y) \in \Gamma_L$ and $(z_0 = z_R, y_0) \in \Gamma_R$. Similarly, $G^{\mathbf{S}_{22}}_{nm}$, and $G^{\mathbf{S}_{12}}_{nm}$ need to be defined. The integral forms of $G^{\mathbf{S}_{11}}_{nm}$, $G^{\mathbf{S}_{21}}_{nm}$, $G^{\mathbf{S}_{22}}_{nm}$, and $G^{\mathbf{S}_{12}}_{nm}$ are identical, given as $\iint \chi_m(y)G(z, y, z_0, y_0)\chi_n(y_0)dydy_0$, except for the differences in their domains of integration, as specified in Table II.

Equation (32) can then be used to estimate S^{nm}_{21} for the four cases described earlier, where the nature of the incident and transmitted modes varies between propagating and evanescent. The estimated results are provided in Table III.

On comparing Table I with Table III, it is observed that for $\mathbf{S}^{nm}_{21}$ elements involving transmitted propagating modes, there is an additional exponential phase term, $e^{-iz_Rk_z^{(n)}}$, arising from the $\phi_n^+(z_0 = z_R)$ term in Eq. (32). The same methodology is applied to estimate the other S-matrix components, $\mathbf{S}_{22}$ (given in Table IV) and $\mathbf{S}_{12}$ (given in Table V). Detailed derivations are provided in Sec VI of the Supplemental Material [24]. for the sake of conciseness in this paper. For evaluating $\mathbf{S}^{nm}_{22}$ and $\mathbf{S}^{nm}_{12}$, incident wave propagates from the right side onto Γ_R. Consequently, the total field on Γ_R consists of both the incident wave and the reflected wave. On the other hand, the total field on Γ_L corresponds to the transmitted wave propagating to the left side of the disorder. Tables I, III, IV, and V

TABLE V. Elements of $\mathbf{S}_{12}$.

Inc(m)	Trans(n)	$\mathbf{S}^{nm}_{12}$
pr	pr	$2i\sqrt{k_z^{(m)}}\sqrt{k_z^{(n)}}e^{-iz_Rk_z^{(m)}}G^{\mathbf{S}_{12}}_{nm}$
ev	ev	$-2\sqrt{\lvert k_z^{(m)}\rvert}\sqrt{\lvert k_z^{(n)}\rvert}G^{\mathbf{S}_{12}}_{nm}$
pr	ev	$2i\sqrt{k_z^{(m)}}\sqrt{\lvert k_z^{(n)}\rvert}e^{-iz_Rk_z^{(m)}}G^{\mathbf{S}_{12}}_{nm}$
ev	pr	$-2\sqrt{\lvert k_z^{(m)}\rvert}\sqrt{k_z^{(n)}}G^{\mathbf{S}_{12}}_{nm}$

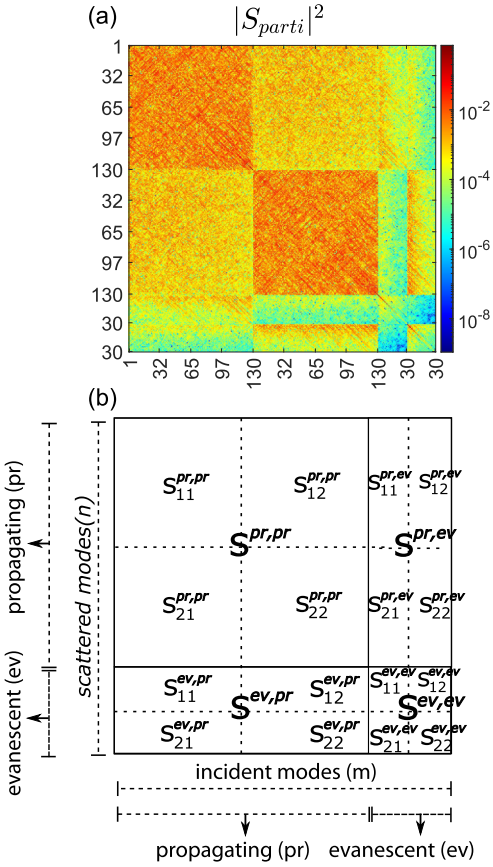


FIG. 3. Partitioned S-matrix. (a) Partitioned S-matrix, referred to as S_{parti}, which rearranges the numerically estimated S-matrix given in Fig. 2(a). The method by which the rearrangement is done is explained in Appendix A. (b) Schematic of various submatrices contained within the corresponding partitioned S-matrix. The superscripts (pr: propagating, ev: evanescent) on the various S-matrix components denote the nature of the scattered and the incident modes. The first superscript (on the left) denotes the nature of the scattered modes and the second superscript (on the right) refers to the nature of the incident modes.

summarize the main results of this section. The S-matrix, estimated numerically using the analytic expressions provided in these tables, is shown in Fig. 2(a).

IV. VERIFICATION OF THE GENERALIZED RECIPROCITY AND UNITARITY PROPERTIES

In this section, the generalized reciprocity relations [16,32] are summarized for the Landauer-waveguide geometry by comparing the expressions for $\mathbf{S}_{11}, \mathbf{S}_{21}, \mathbf{S}_{22}$, and $\mathbf{S}_{12}$ between Tables I, III, IV, and V, respectively. By comparing the expressions given in the first two rows of all the tables, where m and n are either both propagating or both evanescent, we obtain $\mathbf{S}_{11}^{nm} = \mathbf{S}_{11}^{mn}$, $\mathbf{S}_{22}^{nm} = \mathbf{S}_{22}^{mn}$, and $\mathbf{S}_{21}^{nm} = \mathbf{S}_{12}^{mn}$. This arises from the reciprocity symmetry of the perturbed Green's function, such that $G(r, r_0) = G(r_0, r)$, implying $G_{nm} = G_{mn}$. On the other hand, when $m \leqslant M_{\text{pr}}$ and $n > N_{\text{pr}}$, the relations $\mathbf{S}_{11}^{mn} = i\mathbf{S}_{11}^{nm}$, $\mathbf{S}_{22}^{mn} = i\mathbf{S}_{22}^{nm}$, $\mathbf{S}_{12}^{mn} = i\mathbf{S}_{21}^{nm}$, and $\mathbf{S}_{21}^{mn} = i\mathbf{S}_{12}^{nm}$ hold, requiring the inclusion of a factor of i. Similarly, when $m > M_{\text{pr}}$ and $n \leqslant N_{\text{pr}}$, we have $\mathbf{S}_{11}^{mn} = -i\mathbf{S}_{11}^{nm}$, $\mathbf{S}_{22}^{mn} = -i\mathbf{S}_{22}^{nm}$, $\mathbf{S}_{12}^{mn} = -i\mathbf{S}_{21}^{nm}$, and $\mathbf{S}_{21}^{mn} = -i\mathbf{S}_{12}^{nm}$, necessitating the inclusion of a factor of $-i$.

In order to numerically verify these relations, the matrix representation of the same relations is used, which is explained as follows. For the matrix representation of the reciprocity and unitarity relations, the partitioned S-matrix ($\mathbf{S}_{\text{parti}}$) has been defined [32] for convenience. $\mathbf{S}_{\text{parti}}$ rearranges the S-matrix, defined in Eq. (20), into the following block-matrix form:

$$\begin{pmatrix} \mathbf{c}_{\text{out}}^{\text{pr}} \\ \mathbf{c}_{\text{out}}^{\text{ev}} \end{pmatrix} = \underbrace{\begin{bmatrix} \mathbf{S}^{\text{pr,pr}} & \mathbf{S}^{\text{pr,ev}} \\ \mathbf{S}^{\text{ev,pr}} & \mathbf{S}^{\text{ev,ev}} \end{bmatrix}}_{\mathbf{S}_{\text{parti}}} \begin{pmatrix} \mathbf{c}_{\text{inc}}^{\text{pr}} \\ \mathbf{c}_{\text{inc}}^{\text{ev}} \end{pmatrix}, \tag{34}$$

where the terms in the superscripts of the submatrices, pr and ev, represent propagating and evanescent modes, respectively. Such a partitioned S-matrix is shown in Fig. 3(a), formed by rearranging the S-matrix given in Fig. 2(a). The first index in the superscript denotes the nature of the outgoing scattered modes, while the second index denotes the nature of the incident modes as shown in Fig. 3(b). For example, $\mathbf{S}^{\text{pr,ev}}$ contains those elements of the partitioned S-matrix, corresponding to incident evanescent modes and outgoing propagating modes, grouped together as shown in Fig. 3(b). Each of the submatrices $\mathbf{S}^{\text{pr,pr}}$, $\mathbf{S}^{\text{pr,ev}}$, $\mathbf{S}^{\text{ev,pr}}$, and $\mathbf{S}^{\text{ev,ev}}$ can be further subdivided into their corresponding $\mathbf{S}_{11}$, $\mathbf{S}_{12}$, $\mathbf{S}_{21}$, and $\mathbf{S}_{22}$ counterparts. For example, $\mathbf{S}^{\text{pr,ev}}$ represents the block-matrix form

$$\mathbf{S}^{\text{pr,ev}} = \begin{bmatrix} \mathbf{S}_{11}^{\text{pr,ev}} & \mathbf{S}_{12}^{\text{pr,ev}} \\ \mathbf{S}_{21}^{\text{pr,ev}} & \mathbf{S}_{22}^{\text{pr,ev}} \end{bmatrix}, \tag{35}$$

which is schematically shown in Fig. 3(b). The four selection masks used to crop the $\mathbf{S}$-matrix and rearrange it to obtain the partitioned $\mathbf{S}_{\text{parti}}$ matrix components are shown and explained in Fig. 5. Additionally, the coefficients $\mathbf{c}$ given in Eq. (34) associated with the incident (subscript inc) and outgoing (subscript out) scattered eigenmodes are also separated into propagating and evanescent modes.

Using the defined $\mathbf{S}^{\text{pr,pr}}$, $\mathbf{S}^{\text{pr,ev}}$, $\mathbf{S}^{\text{ev,pr}}$, and $\mathbf{S}^{\text{ev,ev}}$ matrices, the analytical forms of the generalized reciprocity relations explained in the beginning of this section are numerically verified as shown in Figs. 6 and 7 in Appendix B. Among these, the important reciprocity relations relevant to this paper are $\mathbf{S}_{12}^{\text{pr,ev}} = i(\mathbf{S}_{21}^{\text{ev,pr}})^T$ and $\mathbf{S}_{12}^{\text{pr,pr}} = (\mathbf{S}_{21}^{\text{pr,pr}})^T$, where T stands for matrix transpose.

Next, we verify the unitarity property of the S-matrix, which implies flux conservation. The compact form [32,33] of the generalized unitarity relation, $\mathbf{S}_{\text{parti}}^{\dagger}\mathbf{I}_{\text{pr}}\mathbf{S}_{\text{parti}} = \mathbf{I}_{\text{pr}} + i\{\mathbf{S}_{\text{parti}}^{\dagger}\mathbf{I}_{\text{ev}} - \mathbf{I}_{\text{ev}}\mathbf{S}_{\text{parti}}\}$, is used for the numerical validation of the relation, as shown in Fig. 8(a) of Appendix C. Here, $\mathbf{I}_{\text{pr}}$ is a matrix with unity only on the diagonal corresponding to the purely propagating portion of $\mathbf{S}_{\text{parti}}$ and zeros elsewhere, as shown in Fig. 8(b). Similarly, $\mathbf{I}_{\text{ev}}$ contains unity elements only on the diagonal corresponding to the evanescent portion of $\mathbf{S}_{\text{parti}}$, as shown in Fig. 8(c). Additional unitarity properties involving modal coefficients $\mathbf{c}_{\text{out}}$ and $\mathbf{c}_{\text{inc}}$ are presented in Appendix D.

V. EVANESCENT MODE TRUNCATION, DISORDER CORRELATION, AND NUMERICAL RESOLUTION

For numerically representing the analytical forms of the eigenmodes and the Green's functions within the computational code, we use numerical grids based on the

finite-difference method. These numerical grids have a finite grid cell size, Δ_z and Δ_y. For the analytical expressions given in the paper to be exact on the grid, Δ_z and Δ_y would need to tend to zero, which is practically not feasible due to the memory and computational processing limitations. Therefore, Δ_z and Δ_y are chosen as a trade-off such that they are small enough to resolve wave states on the grids (especially evanescent eigenmodes), but not so small as to exhaust available memory and the processing capacity. In the limit, lim $\Delta_z, \Delta_y \to 0$, the analytical forms of the wave states and the dispersion relation given in the paper are recovered. For ease of implementation in numeric computations, we set $\Delta_z = \Delta_y = \Delta$ and Δ is chosen to satisfy two conditions. The discretization step size Δ and the total number of transverse modes M_{total} are chosen so as to satisfy both the numerical and physical resolution requirements. The first requirement follows from numerical sampling considerations. For an arbitrarily chosen M_{ev}, $M_{\text{total}} = M_{\text{ev}} + M_{\text{pr}}$ determines the largest transverse wave vector that is resolvable being $k_y^{\max} = M_{\text{total}}\pi/W$. Here, $M_{\text{pr}} \approx 2\eta_{\text{ref}} W/\lambda_0$ is usually fixed for a given W/λ_0 ratio. To ensure adequate numerical resolution of the highest spatial frequency, Δ is chosen such that $k_y^{\max}\Delta \leqslant 1$, which constitutes a conservative sampling criterion. The second requirement is imposed by the scattering property of the disorder, which sets M_{ev} in the particular case when the disorder spatial correlation length ℓ_c goes to be a fraction of the wavelength. The spatial frequency of this subwavelength variation is of the order $k_y \sim 2\pi\eta_{\text{ref}}/\ell_c$. In order to resolve these fine spatial variations, $k_y^{\max} \geqslant 2\pi\eta_{\text{ref}}/\ell_c$. In that case, the M_{total} should be at least $2\eta_{\text{ref}} W/\ell_c$ and $M_{\text{ev}} = 2\eta_{\text{ref}} W/\ell_c - M_{\text{pr}}$. In this scenario, Δ is upgraded such that $k_y^{\max}\Delta \leqslant 1$. This also implies that smaller the ℓ_c, finer discretization is needed, which makes Δ smaller, increasing M_{total} and M_{ev}. This increases the computational memory and processing requirements, making simulations with shorter ℓ_c more computationally demanding. Therefore, users of the code can use these guidelines to manually estimate the required number of evanescent modes and choose an appropriate discretization based on their available memory and computational resources.

Once the suitable M_{total} and Δ are chosen, the finite-difference-based numerical forms of the eigenmodes and Green's functions are constructed (refer to Sec. II of the Supplemental Material [24]). This is to ensure exact conservation of wave flux in the discrete sense. Specifically, the total flux injected by every eigenmode in the numerical form is exactly unity when evaluated as a discrete summation involving the current density, implying $\sum_{y_j} J_z^{(m)}(z_i, y_j)\Delta_y = 1$. This ensures that conservation laws such as unitarity and reciprocity are satisfied exactly to the limit of numerical precision when the various numerical integrations described in this paper are evaluated as discrete summations. Such exact discrete flux conservation comes with the cost that the analytical dispersion relation, $(k_y^{(m)})^2 + (k_z^{(m)})^2 = k_{\text{ref}}^2$, is modified and results in a numerical dispersion relation [Eq. (14) in Sec. II of the Supplemental Material [24]], altering the true form of the dispersion relation. This results in a small numerical dispersion that vanishes as $\Delta \to 0$, which is typical of finite-difference methods.

VI. FOCUSING OF AN EVANESCENT MODE AND UNIVERSAL BACKGROUND TRANSMISSION

This section covers single-mode focusing onto an evanescent mode through the phase conjugation of the transmitted propagating mode generated by the same evanescent mode in a diffusive disorder. Let there be a single evanescent mode (indexed by m') incident only from the right side onto the disorder. The incident evanescent mode is transmitted as a propagating wave traveling to the left side of the disorder. The transmitted propagating wave on the left side can be represented as $\mathbf{c}_{\text{tr}}^{L,\text{pr}} = \mathbf{S}_{12}^{\text{pr,ev}} \mathbb{1}_{m'}^{\text{ev}}$, where $\mathbb{1}_{m'}^{\text{ev}}$ is a column vector selecting the (m')th evanescent mode incidence. For example, $\mathbb{1}_{m'=1}^{\text{ev}} = (1, 0, 0, \ldots, 0)^T$ selects the first evanescent mode. The flux-normalized phase conjugate of $\mathbf{c}_{tr}^{L,\text{pr}}$ is then given as $c_1(\mathbf{c}_{tr}^{L,\text{pr}})^*$, which is incident on the left side of the disorder. Here, c_1 is used for the flux normalization, and its value depends on the (m')th evanescent mode used. The propagating phase conjugate wave incident from the left undergoes transmission on the right side, resulting in

$$\mathbf{c}_{\text{tr}}^{R,\text{ev}} = \mathbf{S}_{21}^{\text{ev,pr}} \left\{ c_1 \left(\mathbf{S}_{12}^{\text{pr,ev}} \right)^* \mathbb{1}_{m'}^{\text{ev}} \right\}, \tag{36a}$$

$$\mathbf{c}_{\text{tr}}^{R,\text{pr}} = \mathbf{S}_{21}^{\text{pr,pr}} \left\{ c_1 \left(\mathbf{S}_{12}^{\text{pr,ev}} \right)^* \mathbb{1}_{m'}^{\text{ev}} \right\}. \tag{36b}$$

Here $\mathbf{c}_{\text{tr}}^{R,\text{ev}}$ contains the complex coefficients for the evanescent component of the transmitted wave on the right side. Similarly, $\mathbf{c}_{\text{tr}}^{R,\text{pr}}$ contains the propagating component, forming the transmitting background. Substituting the reciprocity property (discussed in Sec. IV) that $\mathbf{S}_{12}^{\text{pr,ev}} = i(\mathbf{S}_{21}^{\text{ev,pr}})^T$ into Eq. (36a), we obtain

$$\mathbf{c}_{\text{tr}}^{R,\text{ev}} = -ic_1 \mathbf{S}_{21}^{\text{ev,pr}} \left(\mathbf{S}_{21}^{\text{ev,pr}} \right)^\dagger \mathbb{1}_{m'}^{\text{ev}}. \tag{37}$$

In Eq. (37), the transmitted wave field peaks at the (m')th evanescent mode, resulting in constructive interference leading to focusing as expected and known. Such a focusing scenario is shown in Fig. 4, where the focusing onto a propagating and an evanescent mode is shown separately.

For the remainder of the paper, we discuss the optimal transmission resulting from the background propagating wave formed during evanescent wave focusing. It is important to emphasize that the optimization is performed only over the propagating input modes. Although the target of the focusing is an evanescent mode on the right side of the disorder, the incident wave used for optimization is obtained by phase conjugation of the propagating field generated by that evanescent mode on the opposite side. Therefore, the optimization acts within the propagating subspace, while the evanescent focusing arises indirectly through the coupling between propagating and evanescent modes described by the generalized reciprocity relation. The optimal background transmission associated with the focusing of an evanescent mode is defined as $T_{\text{opt}} = (\mathbf{c}_{tr}^{R,\text{pr}})^\dagger \mathbf{c}_{tr}^{R,\text{pr}}$, where $\mathbf{c}_{tr}^{R,\text{pr}}$ is given in Eq. (36b). Here, T_{opt} corresponds to the total transmitted flux carried by the propagating modes on the right side, while focusing on an evanescent mode optimally, even though the focused evanescent mode by itself does not transmit flux. For diffusive disorders, the ensemble-averaged background transmission $\langle T_{\text{opt}} \rangle$ is observed to be 2/3, similar to the case of the focusing

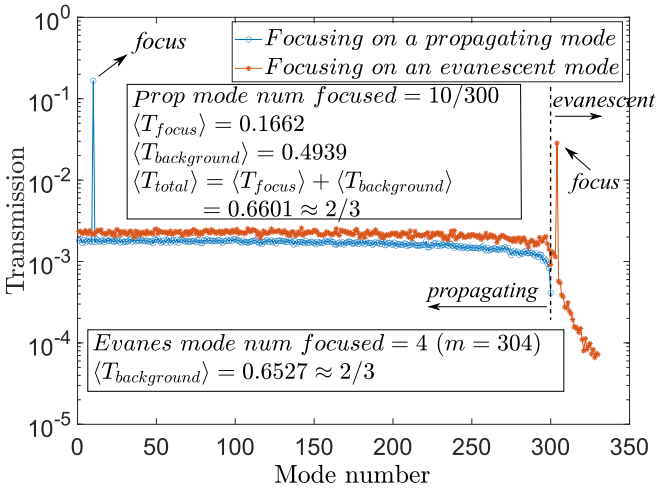


FIG. 4. Ensemble-averaged transmission while focusing via phase conjugation for a collection of cascaded disorders with $\langle \tau_{21}^{\mathrm{pr,pr}} \rangle = 0.1489$. Ensemble-averaged (involving 1000 disordered slabs) distribution of transmission values while focusing onto a propagating mode and an evanescent mode in two separate focusing scenarios. The optimal transmission $\langle T_{\mathrm{opt}} \rangle$ for the focusing of propagating mode is $\langle T_{\mathrm{total}} \rangle = \langle T_{\mathrm{focus}} \rangle + \langle T_{\mathrm{background}} \rangle = 0.6601 \approx 2/3$, which is a universal constant [34] as expected. Here, $\langle \cdots \rangle$ denotes averaging over ensemble. T_{focus} is the transmission only due to the focused mode and $\langle T_{\mathrm{background}} \rangle$ is the total transmission summed over all the modes other than the focus. For the focusing of the evanescent mode, $\langle T_{\mathrm{opt}} \rangle$ is the background transmission $\langle T_{\mathrm{background}} \rangle$ that is a universal constant such that $\langle T_{\mathrm{background}} \rangle = 0.6527 \approx 2/3$. The ensemble of generalized S-matrices is generated by the S-matrix cascading method explained in Sec. IX of the Supplemental Material [24]. and in the user manual for the computational codes.

[34] of propagating modes. The phenomenon can be justified as follows for diffusive disorders.

The transmitted propagating mode $\mathbf{c}_{tr}^{L,\mathrm{pr}}$ on the left, defined previously due to an incident evanescent mode on the right, can also be generated by an equivalent incident propagating mode as follows:

$$\mathbf{c}_{tr}^{L,\mathrm{pr}} = \mathbf{S}_{12}^{\mathrm{pr,ev}} \mathbb{1}_{m'}^{\mathrm{ev}} = c_0 \mathbf{S}_{12}^{\mathrm{pr,pr}} \mathbf{b}_{12,m'}^{\mathrm{pr}}, \tag{38}$$

where the incident propagating column vector $\mathbf{b}_{12,m'}^{\mathrm{pr}}$ is flux normalized as $(\mathbf{b}_{12,m'}^{\mathrm{pr}})^{\dagger} \mathbf{b}_{12,m'}^{\mathrm{pr}} = 1$, and c_0 is a coefficient satisfying Eq. (38) whose value depends on m'. In other words, the transmitted propagating wave after the disorder can be considered indistinguishable, whether it is generated by a single evanescent mode or by an equivalent propagating wave represented by $c_0 \mathbf{b}_{12,m'}^{\mathrm{pr}}$. This equivalent propagating wave, which yields the same transmitted propagating wave due to the given evanescent mode, is a linear combination of the propagating modes addressed by the propagating transmission matrix. Substituting Eq. (38) into Eq. (36b) and using the reciprocity relation $(\mathbf{S}_{12}^{\mathrm{pr,pr}})^{*} = \mathbf{S}_{21}^{\mathrm{pr,pr}\dagger}$, we obtain

$$\begin{aligned} T_{\mathrm{opt}} &= \left(\mathbf{c}_{tr}^{R,\mathrm{pr}}\right)^{\dagger} \mathbf{c}_{tr}^{R,\mathrm{pr}} \\ &= c_0^2 c_1^2 \left(\mathbf{b}_{12,m'}^{\mathrm{pr}}\right)^{T} \mathbf{S}_{21}^{\mathrm{pr,pr}} \left(\mathbf{S}_{21}^{\mathrm{pr,pr}}\right)^{\dagger} \mathbf{S}_{21}^{\mathrm{pr,pr}} \left(\mathbf{S}_{21}^{\mathrm{pr,pr}}\right)^{\dagger} \left(\mathbf{b}_{12,m'}^{\mathrm{pr}}\right)^{*} \\ &= c_0^2 c_1^2 \left(\mathbf{b}_{12,m'}^{\mathrm{pr}}\right)^{T} \mathbf{U}_{21}^{\mathrm{pr,pr}} \left(\boldsymbol{\tau}_{21}^{\mathrm{pr,pr}}\right)^{2} \mathbf{U}_{21}^{\mathrm{pr,pr}\dagger} \left(\mathbf{b}_{12,m'}^{\mathrm{pr}}\right)^{*}, \end{aligned} \tag{39}$$

where the singular value decomposition (SVD) of $\mathbf{S}_{21}^{\mathrm{pr,pr}} = \mathbf{U}_{21}^{\mathrm{pr,pr}} \sqrt{\boldsymbol{\tau}_{21}^{\mathrm{pr,pr}}} \mathbf{V}_{21}^{\mathrm{pr,pr}\dagger}$ is utilized. Here, $\boldsymbol{\tau}_{21}^{\mathrm{pr,pr}}$ is the diagonal matrix containing the eigenchannel transmission coefficients. Next, the ensemble average of T_{opt}, denoted as $\langle T_{\mathrm{opt}} \rangle$, is evaluated. For ensemble averaging, the isotropy [35,36] assumption is applied. This assumption considers $(\boldsymbol{\tau}_{21}^{\mathrm{pr,pr}})^2$ and the remaining terms in Eq. (39) to be statistically uncorrelated during ensemble averaging. Since $\boldsymbol{\tau}_{21}^{\mathrm{pr,pr}}$ obeys the bimodal distribution for diffusive media, $\langle T_{\mathrm{opt}} \rangle$ has the universal value of 2/3 similar to the case of focusing [34] of propagating modes. The associated proof, involving the averaging over unitary groups, is provided in Appendix E. The relation $\langle T_{\mathrm{opt}} \rangle = 2/3$ for evanescent mode focusing is also numerically validated using the developed code, as shown in Fig. 4. Here, the ensemble averaging is performed by generating an ensemble of S-matrices using the S-matrix cascading method [37] (Sec. IX of the Supplemental Material [24]) by randomly shuffling the cascading order. For further details on the numerical validation, refer to the user manual.

VII. CONCLUSION

The analytical description and the associated numerical modeling for estimating the generalized S-matrix are presented from the perspective of classical wave scattering in the Landauer-waveguide geometry. Although the Landauer-waveguide geometry is predominantly used in the context of quantum transport, classical wave scattering methods are intentionally adopted in this paper to make the mesoscopic wave transport theory more accessible to researchers from engineering domains. The authors believe that the presented method offers analytical tractability and generality through the use of Green's functions, despite the fact that the Green's function perturbation method is not the most memory-efficient computational approach among the available algorithms for S-matrix estimation. For a numerically efficient strategy for S-matrix estimation, readers may refer to the recent work by Lin *et al.* [38]. The reduced memory efficiency associated with the Green's function method is mitigated in this paper through the incorporation of the S-matrix cascading method. In this approach, the generalized S-matrices of thinner layers are cascaded to obtain the effective S-matrix of a thicker layer formed by the cascading of these thinner layers. This allows the analysis of a thicker sample to be broken down into a cascade of thinner samples, thereby overcoming the computational burden of solving a large problem in one step. Furthermore, shuffling the order of S-matrices during cascading enables the generation of disorder ensembles, facilitating the estimation of various averages. Since the Green's function perturbation method is employed, starting from the analytical expression for the free-space Green's function with a truncated number of evanescent modes, precise numerical control over the evanescent modes under consideration is achieved. Finally, and most importantly, the usefulness of the model in wavefront shaping applications, specifically for the focusing of an evanescent mode, is demonstrated. The universal background transmission associated with the focusing of an evanescent mode is also discussed. The authors believe that these results and the accompanying code may be of interest to

wavefront shaping researchers studying transport phenomena in general.

ACKNOWLEDGMENTS

We would like to thank Taighde Éireann—Research Ireland for funding this research through S.A.-E.'s Professorship Grant "Novel applications and techniques for *in vivo* optical imaging and spectroscopy" under Grants No. SFI/15/RP/2828 and No. SFI/22/RP-2TF/10293.

M.R. derived the analytical and numerical descriptions of the methodologies presented and developed the associated simulation code packages. B.J. and S.A.-E. supervised M.R.'s Ph.D. project. All authors were involved in the discussion, validation, and interpretation of the results. M.R. wrote the manuscript and the supplementary documents with support from the other authors.

DATA AVAILABILITY

The open-source (MIT license) matlab® codes [39] used for modeling the results are hosted in GitHub [41]. The same repository is also hosted in Zenodo [39]. The saved run data associated with the code packages are also hosted [42]. Users can download the saved run data from Zenodo and place them appropriately within the local GitHub repository to regenerate all the presented results without performing a new computational run from scratch. Alternatively, users can perform a new computational run initializing a new disorder, setting the appropriate flag described in the user manual. The user manual, included in the repository, provides a description of the file structure of the code packages and instructions for their use. The computational simulations were performed on a desktop PC with a configuration of 64 GB of RAM and an eight-core processor (AMD Ryzen 7 2700X). This represents a modest computational setup without the use of specialized high-performance computing resources. Using this configuration, the total run-time required to generate the results presented in this paper was approximately 3.5 h.

APPENDIX A: SELECTION MASKS FOR ESTIMATING PARTITIONED *S*-MATRIX

The selection masks used to rearrange the S-matrix to form the partitioned S-matrix, S_{parti} (shown in Fig. 3), are given in Fig. 5. These selection masks, **Mask**(pr, pr), **Mask**(ev, pr), **Mask**(ev, ev), and **Mask**(pr, ev), have the same dimensions as the S-matrix and contain unity (shown in blue) and zeros (shown in white) as their elements. For instance, **Mask**(pr, pr), shown in Fig. 5, has unity elements when both the incident and scattered modes are propagating. Taking the Hadamard (elementwise) product of the S-matrix with **Mask**(pr, pr) yields $\mathbf{S} \odot \mathbf{Mask}(\text{pr}, \text{pr})$, which isolates the purely propagating contribution of the S-matrix while setting to zero the remaining contribution involving evanescent modes. By discarding the evanescent portion of $\mathbf{S} \odot \mathbf{Mask}(\text{pr}, \text{pr})$ (which was set to zero) and reshaping the matrix to retain only the propagating contribution, we obtain the $\mathbf{S}^{\text{pr,pr}}_{\text{parti}}$ component of the partitioned S-matrix, as given in Eq. (34). Similarly, **Mask**(ev, pr) extracts the portion of the

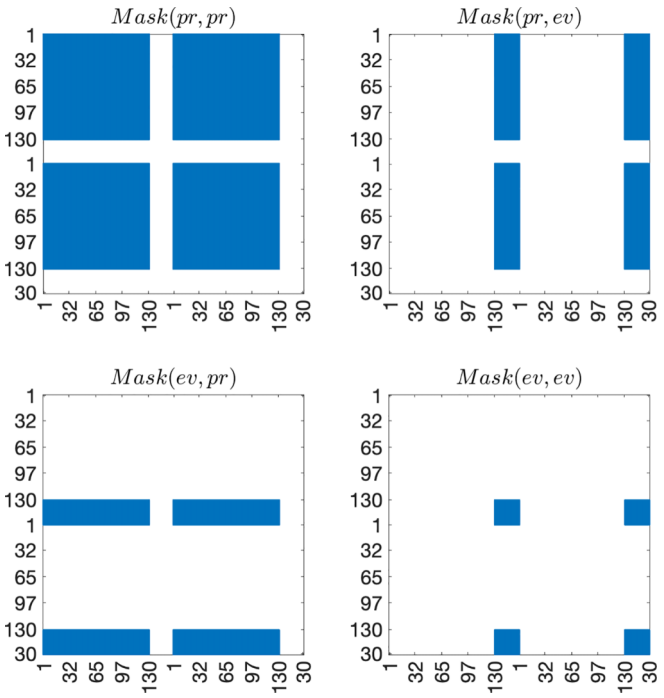


FIG. 5. Plotting the sparsity of the selection mask matrix **Mask** used for generating the partitioned S-matrix, $\mathbf{S}_{\text{parti}}$. Blue color stands for unity and white for zeros. This mask is used to rearrange the S-matrix given in Fig. 2(a) to form the partitioned S-matrix ($\mathbf{S}_{\text{parti}}$) based on Ref. [32]. As an example, **Mask**(ev, pr) selects that part of the S-matrix that contains only modes such that the incident modes are propagating and the scattered being evanescent as explained in Sec. IV.

S-matrix where the incident modes are propagating and the scattered modes are evanescent, yielding $\mathbf{S}^{\text{ev,pr}}_{\text{parti}}$. Analogously, **Mask**(ev, ev) extracts the purely evanescent contribution of the S-matrix, while **Mask**(pr, ev) extracts the contribution where the incident modes are evanescent and the scattered modes are propagating, yielding $\mathbf{S}^{\text{pr,ev}}_{\text{parti}}$. Using these four masks, $\mathbf{S}_{\text{parti}}$ is constructed.

APPENDIX B: NUMERICAL VALIDATION OF THE RECIPROCITY RELATIONS

The generalized reciprocity relations are first validated in an absolute sense, as shown in Fig. 6, where the absolute differences between various submatrices of the partitioned scattering matrix S are displayed. These differences are found to be on the order of 10^{-15}, which corresponds to the numerical precision limit of double-precision floating-point arithmetic. To further quantify the accuracy of the reciprocity relations, we evaluate the corresponding relative error, which is presented in Fig. 7. For example, the relative error matrix associated with the reciprocity condition of $\mathbf{S}^{\text{pr,pr}}$ is defined as

$$\frac{|\mathbf{S}^{\text{pr,pr}} - (\mathbf{S}^{\text{pr,pr}})^T|}{\max\limits_{\text{elementwise}} (|\mathbf{S}^{\text{pr,pr}}|, |(\mathbf{S}^{\text{pr,pr}})^T|)}, \tag{B1}$$

where $\max\limits_{\text{elementwise}}$ denotes the elementwise maximum and all operations are understood in an entrywise sense. The resulting

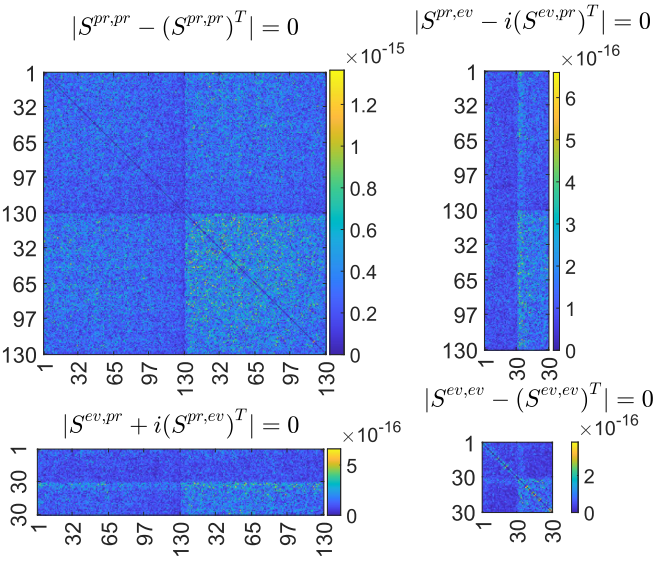


FIG. 6. Numerical validation of the generalized reciprocity relations. Plotting the magnitude of the numerically estimated generalized reciprocity relations in terms of $\mathbf{S}_{\text{parti}}$. The modulus terms on the left-hand side of the reciprocity relations are plotted, whose magnitudes are on the order of 10^{-15}, approximately equal to zero. T stands for matrix transpose.

relative error is found to be on the order of 10^{-12}, as shown in Fig. 7, confirming that the generalized reciprocity relations are satisfied to within the limits of numerical precision.

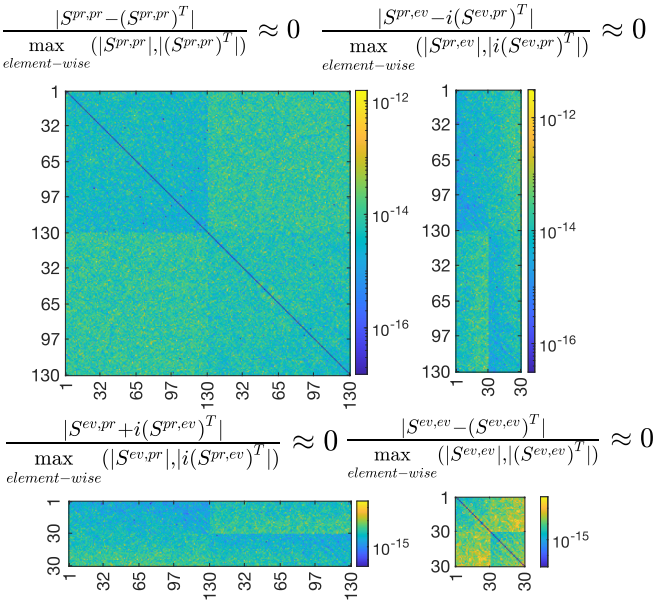


FIG. 7. Relative error of the numerically estimated generalized reciprocity relations. Relative errors are plotted as matrices and the $\max_{\text{elementwise}}$ in the denominator denotes the elementwise maximum and all operations are understood in an entrywise sense. Maximum relative error is on the order of 10^{-12}.

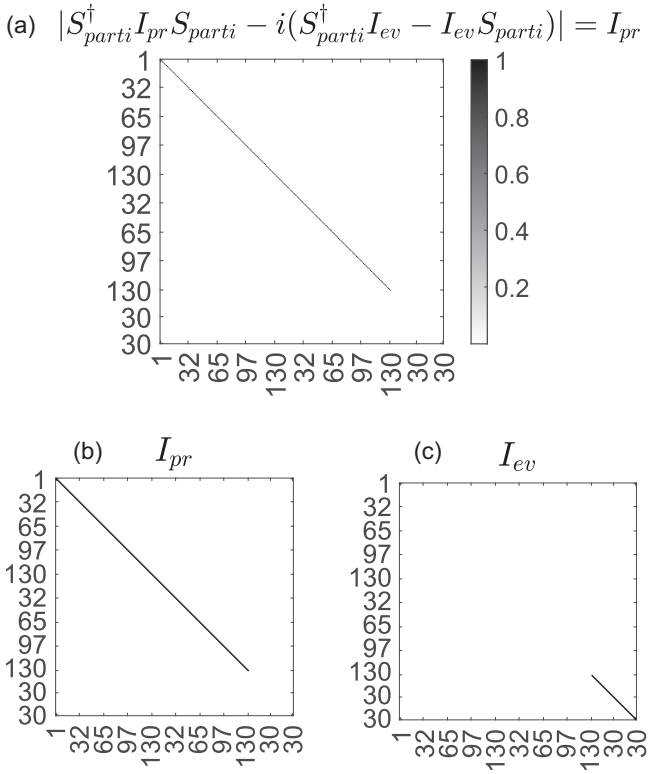


FIG. 8. Numerical validation of the generalized unitarity relations. (a) Plotting the magnitude of the numerically estimated generalized unitarity relation based on the analytical result given in Refs. [32,33]. The modulus term on the left-hand side of the unitarity relation is plotted. The nonzero diagonal elements inside the modulus term on the left-hand side (shown in black color) are all unities and the magnitude of all the other elements are on the order of 10^{-13}, approximated to zero. † stands for the conjugate transpose. Plotting the sparsity of the matrices (b) $\mathbf{I}_{\text{pr}}$ and (c) $\mathbf{I}_{\text{ev}}$ defined in relation to $\mathbf{S}_{\text{parti}}$ used in the unitarity relation (black color stands for unity and white for zeros).

APPENDIX C: NUMERICAL VALIDATION OF THE UNITARITY RELATIONS

The compact form [32,33] of the generalized unitary relation, $\mathbf{S}^{\dagger}_{\text{parti}}\mathbf{I}_{\text{pr}}\mathbf{S}_{\text{parti}} = \mathbf{I}_{\text{pr}} + i\{\mathbf{S}^{\dagger}_{\text{parti}}\mathbf{I}_{\text{ev}} - \mathbf{I}_{\text{ev}}\mathbf{S}_{\text{parti}}\}$, is the combination of the following relations: $(\mathbf{S}^{\text{pr,pr}})^{\dagger}\mathbf{S}^{\text{pr,pr}} = \mathbf{I}$, $(\mathbf{S}^{\text{pr,pr}})^{\dagger}\mathbf{S}^{\text{pr,ev}} = i(\mathbf{S}^{\text{ev,pr}})^{\dagger}$, and $(\mathbf{S}^{\text{pr,ev}})^{\dagger}\mathbf{S}^{\text{pr,ev}} = i\{(\mathbf{S}^{\text{ev,ev}})^{\dagger} - \mathbf{S}^{\text{ev,ev}}\}$. Such a compact form is used to verify the unitary property for the numerically estimated partitioned S-matrix as given in Fig. 8(a). The nonzero diagonal elements inside the modulus term on the left-hand side (shown in black color) are all unities and the magnitude of all the other elements are on the order of 10^{-13}, close to zero. $\mathbf{I}_{\text{pr}}$ and $\mathbf{I}_{\text{ev}}$ are given in Figs. 8(b) and 8(c). For additional numerical verification involving the expanded forms of the compact unitarity relation, refer to Fig. S3 in Sec. VIII of the Supplemental Material [24].

APPENDIX D: ADDITIONAL UNITARITY PROPERTIES

Flux conservation in terms of the modal coefficients given in Eq. (34) is explained next. The complex vectors $\mathbf{c}_{\text{inc}}$ and $\mathbf{c}_{\text{out}}$, with their elements being the complex modal coefficients

defined before, are defined as follows:

$$\mathbf{c}_{\rm inc} = \begin{pmatrix} \mathbf{c}_{\rm inc}^{+,L} \\ \mathbf{c}_{\rm inc}^{-,R} \end{pmatrix} \quad \text{and} \quad \mathbf{c}_{\rm out} = \begin{pmatrix} \mathbf{r}_{\rm out}^{-,L} \\ \mathbf{t}_{\rm out}^{+,R} \end{pmatrix}, \tag{D1}$$

where $\mathbf{c}_{\rm inc}^{+,L}$ is the column vector containing the modal coefficients of the right-going (+) incident wave incident on Γ_L. Similarly, the column vector $\mathbf{c}_{\rm inc}^{-,R}$ contains the modal coefficients of the left-going (−) incident wave incident on Γ_R. Furthermore, $\mathbf{r}_{\rm out}^{-,L}$ is the column vector containing the modal coefficients of the outgoing wave emerging from Γ_L, due to the wave incidence from both the left and right sides of the disorder. Likewise, $\mathbf{t}_{\rm out}^{+,R}$ is the column vector containing the modal coefficients of the outgoing wave emerging from Γ_R due to the wave incidence from both the left and right sides of the disorder. The propagating and evanescent components of $\mathbf{c}_{\rm inc}$ can be separated into $\mathbf{c}_{\rm inc}^{\rm pr}$ and $\mathbf{c}_{\rm inc}^{\rm ev}$, respectively [which are used in Eq. (34)], as follows:

$$\mathbf{c}_{\rm inc}^{\rm pr} = \begin{pmatrix} \mathbf{c}_{\rm inc}^{+,L,{\rm pr}} \\ \mathbf{c}_{\rm inc}^{-,R,{\rm pr}} \end{pmatrix} \quad \text{and} \quad \mathbf{c}_{\rm inc}^{\rm ev} = \begin{pmatrix} \mathbf{c}_{\rm inc}^{+,L,{\rm ev}} \\ \mathbf{c}_{\rm inc}^{-,R,{\rm ev}} \end{pmatrix}. \tag{D2}$$

Similarly, the propagating and evanescent components of $\mathbf{c}_{\rm out}$ can be separated into $\mathbf{c}_{\rm out}^{\rm pr}$ and $\mathbf{c}_{\rm out}^{\rm ev}$.

The flux conservation method presented in Refs. [16,32] can be applied to the modal coefficients. It states that the incident flux, $F_{\rm inc} = \int_0^W \Im\mathfrak{m}\{\tilde{E}_{\rm inc}^* \frac{\partial}{\partial z}\tilde{E}_{\rm inc}\}dy$, must equal the outgoing flux, $F_{\rm out} = \int_0^W \Im\mathfrak{m}\{\tilde{E}_{\rm out}^* \frac{\partial}{\partial z}\tilde{E}_{\rm out}\}dy$, such that $F_{\rm inc} = F_{\rm out}$. This leads to the following generalized flux conservation relation for the Landauer-waveguide geometry:

$$\left(\mathbf{c}_{\rm inc}^{\rm pr}\right)^\dagger \mathbf{c}_{\rm inc}^{\rm pr} - \left(\mathbf{c}_{\rm out}^{\rm pr}\right)^\dagger \mathbf{c}_{\rm out}^{\rm pr} = i\left\{\left(\mathbf{c}_{\rm inc}^{\rm ev}\right)^\dagger \mathbf{c}_{\rm out}^{\rm ev} - \left(\mathbf{c}_{\rm out}^{\rm ev}\right)^\dagger \mathbf{c}_{\rm inc}^{\rm ev}\right\}. \tag{D3}$$

This obtained relation is the discrete version (for the Landauer-waveguide geometry) of the relation given in Eq. (11) of Ref. [16] and Eq. (17) of Ref. [32], which were defined for a different geometry involving a continuous angular spectrum representation. The obtained relation generalizes the well-known flux conservation involving only propagating modes, given as $(\mathbf{c}_{\rm inc}^{\rm pr})^\dagger \mathbf{c}_{\rm inc}^{\rm pr} = (\mathbf{c}_{\rm out}^{\rm pr})^\dagger \mathbf{c}_{\rm out}^{\rm pr}$. For the physical interpretation of the relation given in Eq. (D3) in terms of counterpropagating interference of evanescent modes (on the right-hand side), one may refer to the original proposition in Ref. [16] and the discussions in Refs. [32,40].

In the case of purely propagating incident and scattered modes, where the incident wave modes exist only on the left side of the disorder, a portion of the relation $(\mathbf{S}_{\rm parti}^{\rm pr,pr})^\dagger \mathbf{S}_{\rm parti}^{\rm pr,pr} = \mathbf{I}$ leads to the well-known trace formula [10] for transmission and reflection averaged over different modes, $T_{\rm pr} = (1/M_{\rm pr})\mathbf{Tr}\{(\mathbf{S}_{21}^{\rm pr,pr})^\dagger \mathbf{S}_{21}^{\rm pr,pr}\}$ and $R_{\rm pr} = (1/M_{\rm pr})\mathbf{Tr}\{(\mathbf{S}_{11}^{\rm pr,pr})^\dagger \mathbf{S}_{11}^{\rm pr,pr}\}$, such that $T_{\rm pr} + R_{\rm pr} = 1$. Here, $\mathbf{Tr}$ denotes the trace of the matrix. For a purely evanescent incident wave, the scenario differs, as described below. In the case of incident evanescent wave modes (existing only on the left side of the disorder) and using the generalized unitarity relation $(\mathbf{S}_{\rm parti}^{\rm pr,ev})^\dagger \mathbf{S}_{\rm parti}^{\rm pr,ev} = i\{(\mathbf{S}_{\rm parti}^{\rm ev,ev})^\dagger - \mathbf{S}_{\rm parti}^{\rm ev,ev}\}$, the following holds:

$$\frac{1}{M_{\rm ev}}\mathbf{Tr}\left\{\mathbf{S}_{21}^{\rm pr,ev\dagger}\mathbf{S}_{21}^{\rm pr,ev}\right\} + \frac{1}{M_{\rm ev}}\mathbf{Tr}\left\{\mathbf{S}_{11}^{\rm pr,ev\dagger}\mathbf{S}_{11}^{\rm pr,ev}\right\} = \frac{2}{M_{\rm ev}}\Im\mathfrak{m}\left\{\mathbf{Tr}\left\{\mathbf{S}_{11}^{\rm ev,ev}\right\}\right\}. \tag{D4}$$

This can be considered as the optical theorem for the Landauer-waveguide geometry involving evanescent wave incidence, where the imaginary part of the sum of backscattered evanescent reflection coefficients, along the same direction of the incident evanescent modes, determines the outgoing propagating wave intensity.

APPENDIX E: PROOF THAT $\langle T_{\rm opt}\rangle = 2/3$ FOR EVANESCENT WAVE FOCUSING

The goal of this Appendix is to prove that for diffusive disorders, the ensemble average of $T_{\rm opt}$ given in Eq. (39),

$$\langle T_{\rm opt}\rangle = \left\langle c_0^2 c_1^2 \left(\mathbf{b}_{12,m'}^{\rm pr}\right)^T \mathbf{U}_{21}^{\rm pr,pr}\left(\boldsymbol{\tau}_{21}^{\rm pr,pr}\right)^2 \mathbf{U}_{21}^{\rm pr,pr\dagger}\left(\mathbf{b}_{12,m'}^{\rm pr}\right)^*\right\rangle = 2/3. \tag{E1}$$

Using summation indices, the above equation can also be represented as

$$\langle T_{\rm opt}\rangle = \left\langle c_1^2 c_0^2 \sum_{m_1}\sum_{m_2}\sum_{m_3} \left\{\mathbf{b}_{12,m'}^{\rm pr}\right\}_{m_1,1}\left\{\mathbf{b}_{12,m'}^{\rm pr}\right\}_{m_3,1}^* \times \left\{\mathbf{U}_{21}^{\rm pr,pr}\right\}_{m_1,m_2}\left\{\left(\mathbf{U}_{21}^{\rm pr,pr}\right)^*\right\}_{m_3,m_2}\left\{\left(\boldsymbol{\tau}_{21}^{\rm pr,pr}\right)^2\right\}_{m_2,m_2}\right\rangle. \tag{E2}$$

Taking the isotropy assumption,

$$\langle T_{\rm opt}\rangle = \left\langle c_1^2 c_0^2\right\rangle \sum_{m_1}\sum_{m_2}\sum_{m_3} \left\langle\left\{\mathbf{b}_{12,m'}^{\rm pr}\right\}_{m_1,1}\left\{\mathbf{b}_{12,m'}^{\rm pr}\right\}_{m_3,1}^*\right\rangle \times \left\langle\left\{\mathbf{U}_{21}^{\rm pr,pr}\right\}_{m_1,m_2}\left\{\left(\mathbf{U}_{21}^{\rm pr,pr}\right)^*\right\}_{m_3,m_2}\right\rangle\left\langle\left\{\left(\boldsymbol{\tau}_{21}^{\rm pr,pr}\right)^2\right\}_{m_2,m_2}\right\rangle. \tag{E3}$$

As per Sec. 3 of Ref. [35], $Q_{b\beta}^{a\alpha} = \langle \mathbf{U}_{b\beta}(\mathbf{U}_{a\alpha})^*\rangle = \delta_{ab}\delta_{\alpha\beta}/M_{\rm pr}$, where δ is the Kronecker delta function, and denoting $\sum_{m_2}\{(\boldsymbol{\tau}_{21}^{\rm pr,pr})^2\}_{m_2,m_2} = T_2$, $\langle T_{\rm opt}\rangle$ can be simplified as

$$\langle T_{\rm opt}\rangle = \left\langle c_1^2 c_0^2\right\rangle \sum_{m_1}\sum_{m_3} \left\langle\left\{\mathbf{b}_{12,m'}^{\rm pr}\right\}_{m_1,1}\left\{\mathbf{b}_{12,m'}^{\rm pr}\right\}_{m_3,1}^*\right\rangle \times \left(\frac{\delta_{m_1,m_3}}{M_{\rm pr}}\right)\langle T_2\rangle. \tag{E4}$$

As $(\mathbf{b}_{12,m'}^{\rm pr})^\dagger \mathbf{b}_{12,m'}^{\rm pr} = 1$, $\langle T_{\rm opt}\rangle$ is simplified as

$$\langle T_{\rm opt}\rangle = \left\langle c_1^2 c_0^2\right\rangle \langle T_2\rangle / M_{\rm pr}. \tag{E5}$$

It can be shown (given toward the end of this Appendix) that $\langle c_1^2 c_0^2\rangle = 1/\langle\tau_{\rm avg}\rangle$, where $\tau_{\rm avg}$ is the numerical average of the eigenchannel transmission coefficients contained in the diagonal of the matrix $\boldsymbol{\tau}_{21}^{\rm pr,pr}$. For the bimodal eigenchannel transmission coefficient distribution, $\langle T_2\rangle = 2g/3$, where $g = M_{\rm pr}\langle\tau_{\rm avg}\rangle$ is the optical conductance. Substituting these relations in Eq. (E5), we get $\langle T_{\rm opt}\rangle = 2/3$, which is a universal constant.

For the completeness of the proof, $\langle c_1^2 c_0^2\rangle = 1/\langle\tau_{\rm avg}\rangle$ is derived as follows. As given in the first paragraph of Sec. VI, the flux-normalized propagating phase conjugate wave incident on the left side of the disorder to create an evanescent focus on the right is represented as $c_1(c_{tr}^{L,{\rm pr}})^* = c_1(\mathbf{S}_{12}^{\rm pr,ev})^* \mathbb{1}_{m'}^{\rm ev}$. However, it was seen that $(\mathbf{S}_{12}^{\rm pr,ev})^* \mathbb{1}_{m'}^{\rm ev} = c_0(\mathbf{S}_{12}^{\rm pr,pr})^*(\mathbf{b}_{12,m'}^{\rm pr})^*$.

As flux conservation implies $(c_1(\mathbf{c}_{tr}^{L,\mathrm{pr}})^*)^\dagger(c_1(\mathbf{c}_{tr}^{L,\mathrm{pr}})^*) = 1$, it leads to

$$c_1^2 c_0^2 \left(\mathbf{b}_{12,m'}^{\mathrm{pr}}\right)^T \left(\mathbf{S}_{12}^{\mathrm{pr,pr}}\right)^T \left(\mathbf{S}_{12}^{\mathrm{pr,pr}}\right)^* \left(\mathbf{b}_{12,m'}^{\mathrm{pr}}\right)^* = 1. \tag{E6}$$

Using the reciprocity relation that $(\mathbf{S}_{12}^{\mathrm{pr,pr}})^T(\mathbf{S}_{12}^{\mathrm{pr,pr}})^* = \mathbf{S}_{21}^{\mathrm{pr,pr}}\mathbf{S}_{21}^{\mathrm{pr,pr}\,\dagger}$ and implementing the SVD of $\mathbf{S}_{21}^{\mathrm{pr,pr}}$,

$$c_1^2 c_0^2 \left(\mathbf{b}_{12,m'}^{\mathrm{pr}}\right)^T \mathbf{U}_{21}^{\mathrm{pr,pr}} \boldsymbol{\tau}_{21}^{\mathrm{pr,pr}} \left(\mathbf{U}_{21}^{\mathrm{pr,pr}}\right)^\dagger \left(\mathbf{b}_{12,m'}^{\mathrm{pr}}\right)^* = 1. \tag{E7}$$

Taking the ensemble averaging with the isotropy assumption and using the summation indices,

$$\left\langle c_1^2 c_0^2 \right\rangle \sum_{m_3} \sum_{m_2} \sum_{m_1} \left\langle \left\{\mathbf{b}_{12,m'}^{\mathrm{pr}}\right\}_{m_1,1} \left\{\mathbf{b}_{12,m'}^{\mathrm{pr}}\right\}_{m_3,1}^* \right\rangle \times \left\langle \left\{\mathbf{U}_{21}^{\mathrm{pr,pr}}\right\}_{m_1,m_2} \left\{\mathbf{U}_{21}^{\mathrm{pr,pr}}\right\}_{m_3,m_2}^* \right\rangle \left\langle \left\{\boldsymbol{\tau}_{21}^{\mathrm{pr,pr}}\right\}_{m_2,m_2} \right\rangle = 1. \tag{E8}$$

Further simplifying, using the averaging over unitary groups,

$$\left\langle c_1^2 c_0^2 \right\rangle \sum_{m_3} \sum_{m_1} \left\langle \left\{\mathbf{b}_{12,m'}^{\mathrm{pr}}\right\}_{m_1,1} \left\{\mathbf{b}_{12,m'}^{\mathrm{pr}}\right\}_{m_3,1}^* \right\rangle \times \left(\frac{\delta_{m_1,m_3}}{M_{\mathrm{pr}}}\right) \left\langle \sum_{m_2} \left\{\boldsymbol{\tau}_{21}^{\mathrm{pr,pr}}\right\}_{m_2,m_2} \right\rangle = 1. \tag{E9}$$

As $(\mathbf{b}_{12,m'}^{\mathrm{pr}})^\dagger \mathbf{b}_{12,m'}^{\mathrm{pr}} = 1$,

$$\left\langle c_1^2 c_0^2 \right\rangle (1/M_{\mathrm{pr}})(M_{\mathrm{pr}} \langle \tau_{\mathrm{avg}} \rangle) = 1. \tag{E10}$$

This results in the relation $\langle c_1^2 c_0^2 \rangle = 1/\langle \tau_{\mathrm{avg}} \rangle$, which is used to simplify Eq. (E5).

[1] S. Rotter and S. Gigan, Light fields in complex media: Mesoscopic scattering meets wave control, Rev. Mod. Phys. **89**, 015005 (2017).

[2] I. M. Vellekoop and A. Mosk, Focusing coherent light through opaque strongly scattering media, Opt. Lett. **32**, 2309 (2007).

[3] S. M. Popoff, A. D. Goetschy, S. Liew, A. D. Stone, and H. Cao, Coherent control of total transmission of light through disordered media, Phys. Rev. Lett. **112**, 133903 (2014).

[4] C. W. Hsu, S. F. Liew, A. Goetschy, H. Cao, and A. D. Stone, Correlation-enhanced control of wave focusing in disordered media, Nat. Phys. **13**, 497 (2017).

[5] O. Katz, F. Ramaz, S. Gigan, and M. Fink, Controlling light in complex media beyond the acoustic diffraction-limit using the acousto-optic transmission matrix, Nat. Commun. **10**, 717 (2019).

[6] O. S. Ojambati, H. Yılmaz, A. Lagendijk, A. P. Mosk, and W. L. Vos, Coupling of energy into the fundamental diffusion mode of a complex nanophotonic medium, New J. Phys. **18**, 043032 (2016).

[7] R. Sarma, A. G. Yamilov, S. Petrenko, Y. Bromberg, and H. Cao, Control of energy density inside a disordered medium by coupling to open or closed channels, Phys. Rev. Lett. **117**, 086803 (2016).

[8] N. Bender, A. Yamilov, A. Goetschy, H. Yılmaz, C. W. Hsu, and H. Cao, Depth-targeted energy delivery deep inside scattering media, Nat. Phys. **18**, 309 (2022).

[9] S. M. Popoff, G. Lerosey, R. Carminati, M. Fink, A. C. Boccara, and S. Gigan, Measuring the transmission matrix in optics: An approach to the study and control of light propagation in disordered media, Phys. Rev. Lett. **104**, 100601 (2010).

[10] D. S. Fisher and P. A. Lee, Relation between conductivity and transmission matrix, Phys. Rev. B **23**, 6851 (1981).

[11] A. Goetschy and A. Stone, Filtering random matrices: The effect of incomplete channel control in multiple scattering, Phys. Rev. Lett. **111**, 063901 (2013).

[12] H. Yılmaz, C. W. Hsu, A. Yamilov, and H. Cao, Transverse localization of transmission eigenchannels, Nat. Photonics **13**, 352 (2019).

[13] E. Akkermans and G. Montambaux, *Mesoscopic Physics of Electrons and Photons* (Cambridge University Press, Cambridge, UK, 2007).

[14] G. Lerosey, J. De Rosny, A. Tourin, and M. Fink, Focusing beyond the diffraction limit with far-field time reversal, Science **315**, 1120 (2007).

[15] J. Park, C. Park, K. Lee, Y.-H. Cho, and Y. Park, Time-reversing a monochromatic subwavelength optical focus by optical phase conjugation of multiply-scattered light, Sci. Rep. **7**, 41384 (2017).

[16] R. Carminati, J. J. Sáenz, J.-J. Greffet, and M. Nieto-Vesperinas, Reciprocity, unitarity, and time-reversal symmetry of the *S*-matrix of fields containing evanescent components, Phys. Rev. A **62**, 012712 (2000).

[17] W. Choi, A. P. Mosk, Q.-H. Park, and W. Choi, Transmission eigenchannels in a disordered medium, Phys. Rev. B **83**, 134207 (2011).

[18] S. H. Tseng, A. Taflove, D. Maitland, and V. Backman, Pseudospectral time domain simulations of multiple light scattering in three-dimensional macroscopic random media, Radio Sci. **41**, 2005RS003408 (2006).

[19] C. Liu, L. Bi, R. L. Panetta, P. Yang, and M. A. Yurkin, Comparison between the pseudo-spectral time domain method and the discrete dipole approximation for light scattering simulations, Opt. Express **20**, 16763 (2012).

[20] S. Sukhov, D. Haefner, and A. Dogariu, Coupled dipole method for modeling optical properties of large-scale random media, Phys. Rev. E **77**, 066709 (2008).

[21] M. I. Mishchenko, L. Liu, D. W. Mackowski, B. Cairns, and G. Videen, Multiple scattering by random particulate media: Exact 3D results, Opt. Express **15**, 2822 (2007).

[22] N. Byrnes and M. R. Foreman, Random matrix theory of polarized light scattering in disordered media, Waves Random Complex Medium **36**, 249 (2026).

[23] M. Davy, Z. Shi, and A. Z. Genack, Focusing through random media: Eigenchannel participation number and intensity correlation, Phys. Rev. B **85**, 035105 (2012).

[24] See Supplemental Material at https://link.aps.org/supplemental/10.1103/86th-pl8q for analytical derivations, numerical implementation details, eigenchannel visualizations, and additional validation.

[25] J. Schmitt and G. Kumar, Turbulent nature of refractive-index variations in biological tissue, Opt. Lett. **21**, 1310 (1996).

[26] L. B. Felsen, F. Akleman, and L. Sevgi, Wave propagation inside a two-dimensional perfectly conducting parallel-plate waveguide: Hybrid ray-mode techniques and their visualizations, IEEE Antennas Propag. Mag. **46**, 69 (2004).

[27] R. Carminati and J. C. Schotland, *Principles of Scattering and Transport of Light* (Cambridge University Press, Cambridge, UK, 2021).

[28] Olivier J. F. Martin, A. Dereux, and C. Girard, Iterative scheme for computing exactly the total field propagating in dielectric structures of arbitrary shape, J. Opt. Soc. Am. A **11**, 1073 (1994).

[29] O. J. Martin, C. Girard, and A. Dereux, Generalized field propagator for electromagnetic scattering and light confinement, Phys. Rev. Lett. **74**, 526 (1995).

[30] P. Dömötör, P. Földi, M. G. Benedict, B. W. Shore, and W. P. Schleich, Scattering of a particle with internal structure from a single slit: Exact numerical solutions, New J. Phys. **17**, 023044 (2015).

[31] S. Datta, *Electronic Transport in Mesoscopic Systems* (Cambridge University Press, Cambridge, UK, 1997).

[32] N. Byrnes and M. R. Foreman, Symmetry constraints for vector scattering and transfer matrices containing evanescent components: Energy conservation, reciprocity, and time reversal, Phys. Rev. Res. **3**, 013129 (2021).

[33] Y. V. Gulyaev, Y. N. Barabanenkov, M. Y. Barabanenkov, and S. A. Nikitov, Optical theorem for electromagnetic field scattering by dielectric structures and energy emission from the evanescent wave, Phys. Rev. E **72**, 026602 (2005).

[34] I. M. Vellekoop and A. P. Mosk, Universal optimal transmission of light through disordered materials, Phys. Rev. Lett. **101**, 120601 (2008).

[35] P. Mello, Averages on the unitary group and applications to the problem of disordered conductors, J. Phys. A: Math. Gen. **23**, 4061 (1990).

[36] P. A. Mello and A. D. Stone, Maximum-entropy model for quantum-mechanical interference effects in metallic conductors, Phys. Rev. B **44**, 3559 (1991).

[37] C. Jin, New methods and theory for increasing transmission of light through highly-scattering random media, media, Ph.D. thesis, University of Michigan, Ann Arbor, 2014.

[38] H.-C. Lin, Z. Wang, and C. W. Hsu, Fast multi-source nanophotonic simulations using augmented partial factorization, Nat. Comput. Sci. **2**, 815 (2022).

[39] M. Raju, B. Jayet, and S. Andersson-Engels, MATLAB code packages for "Modeling scattering matrix containing evanescent modes for wavefront shaping applications in disordered media", Zenodo, 2024, https://doi.org/10.5281/zenodo.10963078.

[40] M. Y. Barabanenkov, Y. N. Barabanenkov, Y. V. Gulyaev, and S. Nikitov, Energy emission from evanescent wave and interference of opposite wave streams, Phys. Lett. A **364**, 421 (2007).

[41] https://github.com/michaelraju/Generalized-S-Matrix.

[42] M. Raju, B. Jayet, and S. Andersson-Engels, Dataset for Modeling scattering matrix containing evanescent modes for wavefront shaping applications in disordered media, Data set, Zenodo, 2024, https://doi.org/10.5281/zenodo.10960970.